INVESTIGATION OF THREE ASPECTS OF GLUTAMATE PHYSIOLOGY

by

Delia N. Chiu

A DISSERTATION

Presented to the Neuroscience Graduate Program

and the Oregon Health & Science University

School of Medicine

in partial fulfillment of

the requirements for the degree of

Doctor of Philosophy

September 2014

School of Medicine

Oregon Health & Science University

CERTIFICATE OF APPROVAL

This is to certify that the Ph.D. dissertation of

DELIA CHIU

has been approved on September 10, 2014

Advisor, Craig Jahr, Ph.D.

Member and Chair, Laurence Trussell, Ph.D.

Member, Tianyi Mao, Ph.D.

Member, Stephen Smith, Ph.D.

Member, John Adelman, Ph.D.

Table of Contents

Acknowledgments

First and foremost, I would like to thank my mentor, Craig Jahr, for being a thoughtful, supportive, and inexplicably patient mentor, and for being a true role model. This dissertation marks the end of graduate school but also the beginning of a career in science, and I hope to continue to learn by his example for as long as I am a scientist.

I would like to thank all the members of the Jahr Lab I have been privileged to learn from and work beside: Drs. Vanessa Bender, Brett Carter, Jason Christie, Benjamin Nahir, Jason Pugh, Weinan Sun, and especially Melissa Herman.

I thank Dr. Peter Barr-Gillespie and Dr. Gary Westbrook for inviting me to join the Neuroscience Graduate Program and seeing me through it to the end. And Liz Lawson-Weber, for helping with countless grad school matters.

I am indebted to the many OHSU scientists who taught me over the course of my graduate work; those on the Second Floor of the Vollum Institute, in particular.

Finally, there are several people who were not involved in the work that makes up this dissertation, but to whom I am grateful nonetheless: Dr. Bernd Grünewald, for teaching me how to patch-clamp; Dr. Ora Ohana, who told me there was no room for me in her class and then took me into her lab; and Dr. Daniel Madison at Stanford University, without whom none of this may ever have happened.

Introduction

Excitatory transmission in the vertebrate CNS relies on the release of the amino acid glutamate from the exocytosis of synaptic vesicles at the active zone of presynaptic terminals. Following diffusion across the twenty nanometer wide synaptic cleft, glutamate binds to the cation permeable postsynaptic ionotropic glutamate receptors, AMPA, kainate and NMDA receptors, causing gating and resulting in an excitatory conductance. This conductance leads to depolarization, and can also include influx of calcium, both through NMDA receptors and from activation of voltage-dependent calcium channels; this elevated intracellular calcium can then act as a second messenger in intracellular signaling cascades.

Sufficient depolarization of the somatodendritic compartment of the postsynaptic cell leads to the generation of action potentials in the initial segment of the axon. As the action potential propagates through the axon, it invades axonal boutons, triggering calcium influx through voltage-sensitive calcium channels and the subsequent exocytosis of synaptic vesicles.

Whether action potential invasion of the presynaptic active zone results in exocytosis depends on the release probability (Pr) of the synapse. The Pr, in turn, is dependent on the expression levels, location and species of voltage-sensitive calcium channels, the availability of readily-releasable vesicles, and the history of activity of the synapse, as well as other modulatory mechanisms (Zucker and Regehr, 2002). Both short term and long term alterations in Pr can result from previous levels of activity. In the context of this dissertation, short term increases in Pr resulting from distant, somatodendritic subthreshold activity is a major focus. As with other means of changing presynaptic calcium levels, including repetitive firing, even subthreshold depolarizations can elevate calcium enough to shift Pr to higher levels, as described in the first chapter of the dissertation.

Long term alterations in synaptic efficacy can result from changes in Pr but also in the sensitivity of the postsynaptic membrane via the insertion or depletion of AMPA receptors (Elias and Nicoll, 2007). During the early phases of long term plasticity at many synapses, this postsynaptic change in receptor number predominates. In the case of long term depression and potentiation in the hippocampus, the change in receptor expression has been found to be correlated by volume changes in the postsynaptic spine, on which most excitatory synapses are made (Matsuzaki, Honkura, Ellis-Davies, and Kasai, 2004). Whether the presynaptic side of the synapse also undergoes alterations in morphology is only beginning to be directly addressed (Meyer, Bonhoeffer, and Scheuss, 2014). Based on ultrastructural studies, one would expect that the presynaptic bouton would also change size since there is a significant correlation of the volumes of pre and postsynaptic elements across all synapses (Bourne and Harris, 2008). However, based on electrophysiological studies, there is no evidence that Pr changes, at least during the first hour following the induction protocol. This suggests that, while changes in spine size occur within a minute of the induction protocol, complementary changes in the presynaptic element may be delayed. This question is addressed in the second chapter of the dissertation.

Once glutamate is released into the synaptic cleft, it diffuses to the postsynaptic membrane in a few microseconds and thus reaches the postsynaptic receptors at very high concentrations, in the low millimolar range. At these concentrations, binding to the receptors is almost instantaneous because the binding rates are about 10^7 $M^{-1}s^{-1}$. Thus, activation of synaptic conductances is predominantly rate limited by the first latency of channel opening, which, in the case of AMPA receptors is about a millisecond. Following these very fast events, glutamate diffuses away from the receptors and exits the cleft. As there is little or no degradation of glutamate extracellularly, its concentration in the

extracellular space would continue to climb to toxic levels very rapidly if it were not for the densely packed glutamate transporters, mainly expressed by astrocytes.

The average level of extracellular glutamate, except for brief periods close by sites of exocytotic release, is determined by a balance between the rates of uptake and release. Estimates of this concentration vary over several orders of magnitude, from a few tens of nanomolar to several micromolar. The lower estimates are based on measurements of the degree of neuronal receptor activation whereas the higher estimates are from microdialysis studies and biosensor probes.

One explanation for the divergent concentration estimates is that technical limitations prevent accurate measurement by one – or both – of the techniques. Another possibility that has been suggested is a model of compartmentalization of extracellular glutamate (Moussawi, Riegel, Nair, and Kalivas, 2011). If such compartmentalization exists, different techniques merely sample different compartments, and are both reporting correct estimates for those compartments.

The nucleus accumbens is a part of the midbrain dopaminergic reward circuit. Because drugs of abuse affect neuronal activity in the dopaminergic circuit, there is particular interest in the properties of synaptic transmission in the nucleus accumbens. Several studies have linked behaviors associated with addiction and withdrawal to changes in the steady-state concentration of extracellular glutamate in the nucleus accumbens (Baker et al., 2003; Cornish and Kalivas, 2000; LaLumiere and Kalivas, 2008). In this model, withdrawal of cocaine, for example, decreases activity of the cystine/glutamate antiporter in the nucleus accumbens, which results in a decrease in ambient glutamate. This, in turn, increases excitatory drive to accumbens neurons because of a decrease in presynaptic inhibition via mGluRs on the excitatory inputs to this region. As these accumbens MSN are GABAergic and project to the VTA, the increase release of GABA from accumbens axons inhibits VTA

neurons, decreasing the release of dopamine and this causes withdrawal symptoms. However, the changes in ambient glutamate in this model are in the range of 1-3 μM, which conflict with estimates from hippocampus (25 nM, Herman and Jahr, 2007), we wondered whether this was due to a difference in average concentration or on its distribution. These issues are addressed in the third chapter of the dissertation.

CHAPTER 1.
CA^{2+}-DEPENDENT ENHANCEMENT OF RELEASE BY SUBTHRESHOLD SOMATIC DEPOLARIZATION

Jason M. Christie[1], Delia N. Chiu[1, 2], and Craig E. Jahr[1]

[1]Vollum Institute, Oregon Health and Science University

[2]Neuroscience Graduate Program, Oregon Health and Science University

Portland, OR USA

Address for Correspondence:

Jason M. Christie

Max Planck Florida Institute

5353 Parkside Drive

Jupiter, FL 33458

Phone: (561) 799-8300

Fax: (561) 799-8374

Email: jason.christie@maxplanckflorida.org

Foreword

This study was designed by Dr. Jason Christie as an extension of his investigation of the effect of postsynaptic NMDARs on release (Christie and Jahr, 2008). He performed the paired recordings and many of the individual molecular layer interneuron calcium imaging experiments. I performed the calcium imaging experiments summarized in Figures 1.2 and 1.3. The figures were prepared by Jason. I analyzed my imaging and physiology data in ImageJ and AxoGraph, respectively; all statistics were done by Jason. Craig and I made revisions to the figures and the manuscript, which was drafted by Jason.

Abstract

In many neurons, subthreshold somatic depolarization can spread electrotonically into the axon and modulate subsequent spike-evoked transmission. Although release probability is regulated by intracellular Ca^{2+}, the Ca^{2+}-dependence of this modulatory mechanism has been debated. Using paired recordings from synaptically connected molecular-layer interneurons (MLIs) of the rat cerebellum, we observed Ca^{2+}-mediated strengthening of release following brief subthreshold depolarization of the soma. Two-photon microscopy revealed that, at the axon, somatic depolarization evoked Ca^{2+} influx through voltage-sensitive Ca^{2+} channels (VSCCs) and facilitated spike-evoked Ca^{2+} entry. Exogenous Ca^{2+} buffering diminished these Ca^{2+} transients and eliminated the strengthening of release. Axonal Ca^{2+} entry elicited by subthreshold somatic depolarization also triggered asynchronous transmission that may deplete vesicle availability and thereby temper release strengthening. In this cerebellar circuit, activity-dependent presynaptic plasticity depends on Ca^{2+} elevations resulting from both sub- and suprathreshold electrical activity initiated at the soma.

Introduction

Short-term alteration in the strength of neurotransmission can result from the electrotonic spread of subthreshold depolarization from the soma to presynaptic sites of release on the axon (Alle and Geiger, 2006; Kole, Letzkus, and Stuart, 2007; Shu, Hasenstaub, Duque, Yu, and McCormick, 2006). Mechanisms that trigger or modulate neurotransmission are often mediated through control of VSCCs because the likelihood of vesicle fusion is largely determined by the intracellular [Ca^{2+}]. Although high concentration Ca^{2+} elevations are required to rapidly trigger exocytosis (Bollmann, Sakmann, and Borst, 2000; Schneggenburger and Neher, 2000), low concentration elevations can augment subsequent release via vesicle recruitment, priming, and sensitization (Zucker and Regehr, 2002). Because of their large amplitude, action potentials are efficient triggers for VSCC activation (Bischofberger, Geiger, and Jonas, 2002; Borst and Sakmann, 1996; Brenowitz and Regehr, 2007; Sabatini and Regehr, 1997) and release. However, direct recordings from calyceal nerve terminals show that even slight depolarization can open VSCCs, albeit at low probability, and strengthen subsequent spike-evoked neurotransmission (Awatramani, Price, and Trussell, 2005; Hori and Takahashi, 2009). In contrast, in dentate granule cells of the hippocampus, short-term strengthening of release elicited by modest somatic depolarization may be Ca^{2+}-independent (Alle and Geiger, 2006; Scott, Ruiz, Henneberger, Kullmann, and Rusakov, 2008). Whether somatic depolarization enhances action potential-evoked release by activating axonal VSCCs in inhibitory neurons has not been addressed, although asynchronous release is augmented in a Ca^{2+}-dependent manner in young animals (Trigo et al., 2010).

MLIs of the cerebellum, including stellate and basket cells, make inhibitory GABAergic synapses onto Purkinje cells as well as other MLIs (Palay and Chan-Palay, 1974).

Depolarizing potentials originating in the somatodendritic compartment of MLIs passively propagate into their axonal arbor (Glitsch and Marty, 1999; Mejia-Gervacio et al., 2007) and open VSCCs (Christie and Jahr, 2008). However, action potentials are required to rapidly coordinate release from presynaptic sites, thereby limiting the voltage range for VSCC activation to subthreshold depolarization. Whether axonal Ca^{2+} entry evoked by subthreshold somatic depolarization is sufficient to alter spike-evoked neurotransmission has not been directly determined in MLIs.

Here, we investigated the mechanisms that mediate somatic voltage control of axonal transmitter release between MLIs using paired electrical recording and two-photon laser scanning microscopy (2PLSM). Subthreshold somatic depolarization was sufficient to activate axonal VSCCs, elicit Ca^{2+} influx and strengthen both action potential-evoked and asynchronous transmitter release. Enhancement of release was diminished or eliminated by chelating intracellular Ca^{2+} with EGTA or by blocking VSCCs, indicating that there is a direct connection between somatic voltage-control of neurotransmission and Ca^{2+} entry at the site of release. This suggests that release plasticity elicited by subthreshold somatic depolarization depends on presynaptic VSCCs.

Materials and Methods

Slice preparation

Parasagittal slices from cerebellar vermi were prepared from Sprague Dawley rats (PND 14–20) in accordance with protocols approved by the Oregon Health and Science University Institutional Animal Care and Use Committee. Rats, following isoflurane anesthesia, were decapitated and the cerebellum was isolated. Slices (250–300 μm) were cut on a Leica VT1200S vibrating blade microtome (Leica Instruments, Nussloch, Germany) in an ice-cold solution containing (in mM) 87 NaCl, 25 $NaHO_3$, 2.5 KCl, 1.25 NaH_2PO_4, 7 $MgCl_2$, 0.5 $CaCl_2$, 10 glucose, and 75 sucrose. Slices were subsequently transferred to a holding chamber containing (in mM) 119 NaCl, 26.2 $NaHO_3$, 2.5 KCl, 1 NaH_2PO_4, 2 $MgCl_2$, 1 $CaCl_2$, 11 glucose and maintained at 34°C for 30 min, thereafter, at 22–25°C until use. For whole-cell recording, slices were placed in a submersion chamber and superfused with the same solution (22–25°C) altered by elevating $CaCl_2$ to 1.5 and reducing $MgCl_2$ to 1.5 mM, except where noted. All solutions were oxygenated by pre- or continuous equilibration with carbogen gas (95% O_2, 5% CO_2).

Electrophysiology

Whole-cell recordings were obtained from MLIs identified with gradient-contrast infrared video microscopy (Dodt, Eder, Schierloh, and Zieglgänsberger, 2002) based on their location within the molecular layer and distinct morphology (Palay and Chan-Palay, 1974). Patch pipettes used for current-clamped MLIs contained a solution of (in mM) 128 K-gluconate, 2 KCl, 9 HEPES, 4 $MgCl_2$, 4 NaATP, and 0.5 NaGTP and 9 K_4-BAPTA. For paired recordings, perforated access (Rae, Cooper, Gates, and Watsky, 1991) to the presynaptic MLI was achieved by including amphotericin B (300 μg/ml, previously aliquoted

in DMSO). Alexa Fluor 488 hydrazide (30 μM; Molecular Probes; Eugene, OR) was also included in the pipette to fluorescently monitor the integrity of the perforated recording with light microscopy. If the patch membrane ruptured, resulting in cell fluorescence, recording was terminated. For Ca^{2+}imaging experiments, K_4-BAPTA was replaced with 200 μM Fluo-5F and 13 μM Alexa Fluor 594 hydrazide (Molecular Probes, Eugene, OR). Current-clamped cells were held near −70 mV with constant current injection. Action potentials were stimulated between 0.3 to 0.1 Hz (~25–60 trials per condition). MLIs were voltage-clamped with a pipette solution containing (in mM) 135 CsCl, 10 HEPES, 4 Mg_2ATP, 0.3 NaGTP and 5 EGTA. The holding potential was kept at −60 mV giving rise to inward $GABA_A$R-mediated currents ($E_{Cl^-} \approx 0$ mV). All pipettes had open-tip resistances of 3–12 MΩ.

Electrophysiological potentials and currents were recorded with a Multiclamp 700B amplifier (Molecular Devices, Union City, CA). Electrode series resistance was compensated by bridge balance in current-clamped cells and was uncompensated in the voltage-clamp configuration. Analog signals were filtered at 3–10 kHz and digitized at 20–50 kHz with a 16-bit A/D converter (Instrutech Corp., Port Washington, NY). High access resistance (40–80 MΩ) in the presynaptic perforated recording also likely contributed to filtering and action potential attenuation, though, access often improved during an experiment due to continued partitioning of the antibiotic. Data were collected using custom software (J.S. Diamond) written in IgorPro (Wavemetrics, Lake Oswego, OR) and analyzed using Axograph (Axograph Scientific, Sydney, Australia). $GABA_A$R-mediated synaptic responses were isolated with NBQX (10 μM) and *D*-AP5 (50 μM) (Tocris Cookson, Ellisville, MO) to block fast glutamate receptor-mediated responses. Picrotoxin (100 μM) was also included during imaging experiments to eliminate $GABA_A$R-mediated transmission. EGTA-AM (10–20 μM, Molecular Probes, Eugene, OR), made from a stock 100 mM solution in DMSO, was applied for at least 10 minutes during which data acquisition ceased. Upon resumption,

EGTA-AM was continuously applied until the end of the experiment. In amplified views shown in figures, spontaneous IPSCs that were not time-locked to the presynaptic action potential were blanked prior to averaging for illustrative purposes; events were only included within 1 ms after the action potential peak. In our analysis, however, spontaneous events were left unmodified.

Two-photon laser-scanning microscopy

Fluorescence was monitored with a lab-built 2PLSM using an Olympus (Melville, NY) upright microscope, objective (60X, 1.0 NA), and oil-immersion condenser (1.4 NA). A Ti:sapphire laser (Coherent, Santa Clara, CA) tuned to 810 nm was used for excitation. Emitted green and red fluorescence were simultaneously collected by photomultiplier modules (H8224, Hamamatsu, Hamamatsu City, Japan) in both epi- and transfluorescence pathways using a 565 nm dichroic and 525/50 and 620/60 bandpass filters (Chroma, Battleboro, VT). Images were acquired using ScanImage software (K. Svoboda). Line scans were obtained at 500 Hz. Cells were filled for a minimum of 20 minutes prior to acquisition to allow for dye equilibration (axon varicosities <150 μm from the soma). For varicosities >150 μm from the soma, longer equilibration times were used.

Imaging analysis was performed offline using ImageJ (National Institutes of Health) and Axograph. Fluorescence changes were quantified as increases in green fluorescence normalized to red fluorescence ($\Delta G/R$). Peak amplitude measurements of subthreshold depolarization-evoked Ca^{2+} transients were determined by averaging a 100 ms epoch prior to action potential firing. Alternating trials in which no stimulation occurred were used to subtract background fluorescence levels; the difference reflecting the peak response. The peak of action potential-evoked Ca^{2+} transients were determined from exponential fits of the fluorescence decay following stimulation (measured at $t = 0$). Changes in the peak amplitude

of action potential-evoked responses might be underestimated if the indicator were in the non-linear range. The Ca^{2+} transients evoked by subthreshold depolarization were usually very small. Therefore, for illustrative purposes only, we integrated these responses to accentuate the rise in Ca^{2+} from the baseline noise during the subthreshold stimulus (Fig. 1.2B, 1.3A). This method was not included in any quantification.

Statistical analysis

Reported values are mean ± SEM. Excel (Microsoft, Seattle, WA) and InStat (GraphPad Software) were used for statistical analysis using paired and unpaired t-tests (two-tailed). ANOVA with post-hoc Tukey's tests were used when making multiple comparisons. Differences were considered statistically significant with α values of $p < 0.05$. In figures, asterisks denote statistical significance.

Results

Subthreshold depolarization enhances AP-evoked release

$GABA_A$ receptor ($GABA_AR$)-mediated synaptic transmission was examined between pairs of MLIs in rat cerebellar slices using simultaneous whole-cell recording. Action potentials elicited in presynaptic cells by somatic current injection (100 – 600 pA, 3 – 5 ms) evoked time-locked inward currents in voltage-clamped postsynaptic cells ($E_{Cl^-} \approx 0$ mV) that were blocked by picrotoxin (100 μM; 3.8 ± 1.8 % of control; n = 5). Irreversible rundown of evoked transmission, commonly observed in paired MLI recordings (Vincent and Marty, 1996), was eliminated by presynaptic perforated patch recording (Diana and Marty, 2003) (see Methods). To determine whether somatic depolarization was sufficient to alter the strength of neurotransmission, presynaptic neurons were briefly depolarized from rest (−73.3 ± 0.3 mV; n = 40) to a potential just subthreshold for spiking (−56.1 ± 0.9 mV, 300 ms). This depolarization was followed by action potential stimulation (10 ms delay). IPSCs evoked by action potentials preceded by subthreshold depolarization were larger than interleaved control IPSCs evoked by action potentials alone (121.1 ± 4.8% of control amplitude; n = 40, $p < 0.001$; Fig. 1A). Furthermore, the paired-pulse ratio (PPR = $IPSC_2/IPSC_1$) of IPSCs evoked by two action potentials (250 ms interval; PPR = 1.000 ± 0.064, n = 37; Fig. 1.1A, 1.1B) following subthreshold depolarization was significantly reduced compared to non-depolarized control trials ($p = 0.002$; Fig. 1.1A, 1.1C). This indicates that subthreshold somatic depolarization causes a short-term alteration in presynaptic release resulting from the electrotonic spread of the somatic depolarization into the axon, as observed in other neurons (Alle and Geiger, 2006; Kole et al., 2007; Scott et al., 2008; Shu et al., 2006).

Control recordings included both facilitating and depressing responses (Fig. 1.1C), indicating that synapses between MLIs with different release probabilities co-exist in cerebellum. Synaptic strengthening caused by subthreshold depolarization depended on basal release probability, as the amount of enhancement of $IPSC_1$ was correlated with the PPR measured in control trials (Fig. 1.1D). Depressing synapses, on average, were not altered by subthreshold depolarization ($p = 0.17$). However, there was considerable variability within this group, with some pairs showing release enhancement while others were weakened (Fig. 1.1E). In 3 mM extracellular Ca^{2+} release enhancement caused by subthreshold depolarization was less than in 1.5 mM Ca^{2+} (Fig. 1.1E), but the increase was still significant ($p = 0.03$). High extracellular Ca^{2+}increased release probability, as reflected by larger control IPSCs (peak amplitude 306.0 ± 67.0 and 172.7 ± 22.5 pA, 3.0 and 1.5 mM Ca^{2+}, respectively; $n = 13$ and 40, $p = 0.02$) and paired-pulse depression in all recordings ($n = 11$, Fig. 1.1F). Thus, strengthening of release by subthreshold depolarization is similar to other activity-dependent forms of release enhancement, such as spike-evoked facilitation and augmentation, in that these processes occur more readily in low release probability synapses.

Subthreshold depolarization and presynaptic Ca^{2+} entry

Intracellular Ca^{2+} is known to govern many aspects of transmitter release (Zucker and Regehr, 2002). Therefore, we probed for presynaptic Ca^{2+} elevation evoked by subthreshold somatic depolarization using 2PLSM. MLIs were filled through the whole-cell patch pipette with Alexa Fluor 594 to visualize cell morphology and the Ca^{2+} indicator Fluo-5F to detect intracellular Ca^{2+} transients (Fig. 1.2A). Axon varicosities were targeted for optical recording. These varicosities are known to be hotspots of action potential-evoked Ca^{2+} entry and, therefore, are presumed to be *en passant* sites of release (Christie and Jahr,

2008; Forti, Pouzat, and Llano, 2000; Llano, Tan, and Caputo, 1997; Palay and Chan-Palay, 1974), though it remains possible that these specializations may include non-synaptic sites.

In current-clamped MLIs, subthreshold somatic depolarization (300 ms) often evoked small Ca^{2+} transients in axon varicosities (Fig. 1.2B; ΔSub Ca^{2+}). The amplitude of these Ca^{2+} transients varied across recording sites, including many varicosities without any apparent Ca^{2+} elevation (Fig. 1.2C). However, on average, Ca^{2+} responses were significantly larger than corresponding measurements obtained from interleaved control trials without subthreshold depolarization (ΔG/R −0.0010 ± 0.0004 and 0.0026 ± 0.0010, control and depolarized, respectively; $p < 0.0001$; $n = 35$). In addition, we observed that Ca^{2+}transients evoked by action potentials following subthreshold depolarization were larger than those without prior depolarization (Fig. 1.2B). Subtraction of the Ca^{2+} elevation evoked during the subthreshold depolarization revealed that the facilitation of spike-evoked Ca^{2+} (24.5 ± 4.5% increase in peak amplitude, $p < 0.001$) was not merely the result of the shift in baseline fluorescence, but rather a true enhancement of spike-induced Ca^{2+} influx (Fig. 1.2B; ΔAP Ca^{2+}). The amount of spike-evoked Ca^{2+} facilitation was not correlated with the amplitude of Ca^{2+} influx during subthreshold depolarization (Fig. 1.2C). Whether this indicates that the two components contributing to Ca^{2+} elevation are not causally related is unclear because the extremely small amplitude of the subthreshold response interferes with our ability to accurately measure it. However, in 3 mM extracellular Ca^{2+}, the Ca^{2+} transient resulting from subthreshold depolarization was larger than that in control conditions (Peak ΔG/R 0.0036 ± 0.0008 and 0.0061 ± 0.0030; 1.5 and 3.0 extracellular Ca^{2+}, respectively; $n = 35$ and 74, $p = 0.04$) and was correlated with the facilitation of the spike-induced Ca^{2+} influx ($r^2 = 0.19$; $p = 0.0002$), suggesting that the Ca^{2+} elevation during subthreshold depolarization caused the spike-induced facilitation.

Inhibition of VSCCs by a combination of antagonists (ω-conotoxin MVIIC 1 μM, SNX 0.3 μM, nimodipine 20 μM, and mibefradil 10μM) confirmed that subthreshold depolarization-evoked Ca^{2+} entry occurs through VSCCs (Supplemental Fig. 1.1) as previously reported (Christie and Jahr, 2008). The unblocked component presumably reflects toxin-resistant VSCCs (Forti et al., 2000; Metz, Jarsky, Martina, and Spruston, 2005; Tottene, Moretti, and Pietrobon, 1996), as spike-evoked Ca^{2+} transients were blocked to a similar extent (Supplemental Fig. 1.1B). Subthreshold depolarization-induced facilitation of spike-evoked Ca^{2+} entry was also diminished by VSCC inhibition (8.7 ± 5.0% of control; n = 9, p = 0.002), again suggesting that this facilitation was dependent on an increase in intracellular Ca^{2+} elicited by the preceding subthreshold depolarization.

Release strengthening caused by subthreshold depolarization in MNTB calyceal nerve terminals is inhibited by Ca^{2+} chelation, implying an alteration in an underlying Ca^{2+} elevation (Awatramani et al., 2005; Hori and Takahashi, 2009). In MLI axonal varicosities, depolarization-evoked Ca^{2+} entry was not significantly altered by the cell-permeable Ca^{2+} buffer EGTA-AM (10–20 μM; >10 min; p = 0.08, Fig. 1.3A, 1.3B). However, in many cases subthreshold depolarization did not result in a measurable Ca^{2+}transient (see Fig. 1.2C) and, therefore, an effect of chelation overall could only be determined indirectly, using paired recording (see below). To test for a direct effect of chelation on Ca^{2+} elevation induced by subthreshold depolarization, we focused our analysis on large-amplitude responses (ΔG/R > 0.0050; n = 4; Fig. 1.3A). In this group, EGTA significantly reduced the Ca^{2+} transients (ΔG/R 0.0090 ± 0.0019 and 0.0043 ± 0.0027, control and EGTA, respectively, n = 4, p = 0.03). Facilitation of spike-evoked Ca^{2+} entry following subthreshold depolarization was greatly diminished by EGTA across all cells (Fig. 1.3C), indicating that, even in cases where depolarization did not produce a measurable increase in Ca^{2+}, facilitation of the spike-evoked Ca^{2+} transient was Ca^{2+}-dependent (Borst

and Sakmann, 1998; Cuttle, Tsujimoto, Forsythe, and Takahashi, 1998). EGTA also reduced Ca^{2+} transients evoked by single action potentials alone (70.1 ± 3.3% of control; n = 9, p = 0.008; Fig. 1.3A), suggesting a competition between Fluo-5F and EGTA for Ca^{2+} binding (Atluri and Regehr, 1996), that basal Ca^{2+} levels are sufficient to partially facilitate VSCC opening, or that there was a substantial rundown of VSCC opening.

Enhancement of release is Ca^{2+}-dependent

In paired MLI recordings, the enhancement of $IPSC_1$ by subthreshold depolarization was blocked by EGTA-AM (20 μM; >10 min; 122.2 ± 7.4 and 97.5 ± 6.9% of control amplitude, −EGTA and +EGTA, respectively, n = 9, p = 0.009; Fig. 1.4A, 1.4B). This indicates that the increase in spike-evoked release caused by subthreshold depolarization depends on the EGTA-sensitive Ca^{2+} elevation observed in axon varicosities. The block of release-strengthening by EGTA occurred mainly in recordings showing paired-pulse facilitation in control conditions. On average, IPSCs in depressing cell pairs were unaltered by subthreshold depolarization and remained unchanged with the addition of EGTA (Fig. 1.4B, top; see also Fig. 1.1E). It follows that the magnitude of the EGTA effect was correlated with the control PPR (Fig. 1.4B, bottom). This reinforces the conclusion that subthreshold depolarization differentially affects release at MLI synapses in a release probability-dependent manner.

EGTA did not affect the amplitude of IPSCs evoked without preceding subthreshold depolarization (Fig. 1.4C; IPSC amplitudes 97.5 ± 4.8 and 82.8 ± 11.3% of control; n = 5 and 4, p = 0.47 and 0.16; facilitating, and depressing responses, respectively). This implies that the Ca^{2+} domain responsible for triggering exocytosis is tightly associated with release-competent vesicles (Bucurenciu, Bischofberger, and Jonas, 2010; Bucurenciu, Kulik, Schwaller, Frotscher, and Jonas, 2008). However, EGTA altered the PPR, changing

facilitation to depression, though it had no clear effect on depressing cell pairs (Fig. 1.4C, 1.4D; PPR for depressing cells 0.67 ± 0.09 and 0.97 ± 0.09, control and EGTA, respectively; n = 4, p = 0.13). This suggests that, in basal conditions, residual Ca^{2+} following an initial spike facilitates subsequent release (Atluri and Regehr, 1996) and may mask depression (Dittman, Kreitzer, and Regehr, 2000; Müller, Goutman, Kochubey, and Schneggenburger, 2010). EGTA did not induce a significant change in the PPR in these responses when subthreshold depolarization preceded spiking (PPR 0.79 ± 0.05 and 1.01 ± 0.11 EGTA and +EGTA, respectively; n = 5, p = 0.18), suggesting little additional or underlying modification of release in this condition.

Subthreshold depolarization and asynchronous release

At some synapses, asynchronous release can result from the low concentration of Ca^{2+} remaining after spike firing (Atluri and Regehr, 1998; Lu and Trussell, 2000). In our paired recordings, there was often a small increase in the frequency of asynchronous IPSCs during subthreshold somatic depolarization (Fig. 1.5A) likely caused by the elevation of Ca^{2+} by the depolarizing stimulus. Although in many recordings, spike-evoked IPSCs from unclamped surrounding MLIs likely overwhelmed this small increase in asynchronous transmission, charge integration of averaged postsynaptic currents revealed a difference between control and depolarized trials across cells (Fig. 1.5B). The increase of asynchronous IPSCs by presynaptic somatic depolarization was much clearer when background action potential-driven release from spontaneously firing surrounding cells was blocked with TTX (1 μM) and the stimulus duration was prolonged (150 s; 3 mM extracellular Ca^{2+}; Fig. 1.6A, 1.6B, and 1.6D). Block of VSCCs by Cd^{2+} and Ni^{2+} (100 μM) eliminated depolarization-evoked asynchronous release without affecting basal spontaneous transmission (Fig. 1.6C,

1.6E), demonstrating the connection between somatic depolarization, axonal VSCC activation, and asynchronous release.

Asynchronous release elicited by repetitive firing weakens subsequent action potential-evoked phasic transmission by depleting the pool of readily-releasable vesicles (Lu and Trussell, 2000; Otsu et al., 2004). Vesicle availability may, in part, regulate release strengthening induced by subthreshold depolarization. To explore this idea, we reduced the releasable pool of vesicles with a train of presynaptic action potentials (10 spikes, 60 Hz) and then tested for subthreshold depolarization-induced enhancement of release (Fig. 1.7A). The amplitude of spike-evoked test IPSCs following burst firing was reduced compared to interleaved trials without the burst (77.3 ± 7.0% of control; $n = 10$, $p = 0.05$, Fig. 1.7B), a result consistent with depression induced by vesicle depletion. In addition, burst firing eliminated release-strengthening elicited by subthreshold depolarization (Fig. 1.7A, 1.7C). This indicates that in conditions that diminish the releasable pool of vesicles, subthreshold depolarization is less effective in altering release probability. By extension, asynchronous release elicited by subthreshold depolarization likely limits the strengthening of spike-evoked transmission by depleting the readily-releasable pool of vesicles. This may explain why in some cell pairs (4 of 10) the additive effect of subthreshold depolarization and bursting resulted in a weakening of transmission rather than enhancement (Fig. 1.7A, 1.7C).

Discussion

We report that subthreshold somatic depolarization passively spreads into the axon arbor of MLIs and strengthens subsequent action potential-evoked release of GABA onto neighboring cells. Therefore, subthreshold depolarization enhancement of release is not limited to excitatory neurons, but also includes inhibitory neurons as well. We show that for MLIs, this enhancement of release depends on the opening of VSCCs, which results in Ca^{2+} elevation as well as facilitation of spike-evoked Ca^{2+} influx, a novel finding. An increase in asynchronous release that accompanies the subthreshold depolarization is Ca^{2+}-dependent and may decrease the capacity for release strengthening owing to vesicle depletion. Our results suggests the possibility that subthreshold potentials may modify neurotransmission at synapses throughout the nervous system in a Ca^{2+}-dependent manner, as do other forms of short-term facilitation.

Somatic depolarization and Ca^{2+} influx at sites of release

Axons are not electrotonically isolated from the somatodendritic compartment, but rather support the electrotonic spread of subthreshold somatodendritic potentials (Alle and Geiger, 2006; Christie and Jahr, 2008; Kole et al., 2007; Mejia-Gervacio et al., 2007; Shu et al., 2006). As a result, the open probability of voltage-sensitive ion channels in axons can be modified by somatodendritic depolarization. Our Ca^{2+} measurements indicate that somatic depolarizations electrotonically spread into MLI axons and are sufficient to open VSCCs. Though not directly determined in this report, axonal length constants can exceed 400 μm in some neurons (Alle and Geiger, 2006; Christie and Jahr, 2009; Kole et al., 2007; Shu et al., 2006). This parameter must be convolved with the number and composition of VSCCs at sites of release to determine subthreshold depolarization-mediated Ca^{2+} entry (Li,

Bischofberger, and Jonas, 2007). In calyceal terminals, P/Q-type VSCCs open at low probability following slight depolarization (Awatramani et al., 2005) (≤ 60 mV), an activation range below that previously reported (Borst and Sakmann, 1998; L. G. Wu, Borst, and Sakmann, 1998). Although MLI varicosities express P/Q/N-type channels, among others (Forti et al., 2000), the VSCC subtypes mediating depolarization-evoked Ca^{2+}influx remain unclear. It is possible that low-activation threshold VSCCs, such as R-type channels, preferentially mediate this Ca^{2+}influx, as predicted for hippocampal mossy fiber boutons (Li et al., 2007). It is unknown whether Ca^{2+}-induced Ca^{2+} release from intracellular stores (Llano et al., 2000) contributes to subthreshold depolarization-evoked Ca^{2+}transients.

Subthreshold depolarization not only induces direct influx of Ca^{2+} in MLI axons, but also facilitates action potential-evoked Ca^{2+} entry. This effect is probably dependent on the preceding influx of Ca^{2+}, because both inhibition of VSCCs and Ca^{2+} chelation diminished the facilitation of spike-evoked Ca^{2+} entry. At some synapses, VSCC-mediated currents are enhanced following Ca^{2+} binding by neuronal calcium sensor 1 (NCS-1), which induces shortening of the activation phase of VSCCs (Cuttle et al., 1998; Tsujimoto, Jeromin, Saitoh, Roder, and Takahashi, 2002). VSCC facilitation is elicited by both supra- and subthreshold depolarization-evoked Ca^{2+} elevation and is mitigated by exogenous Ca^{2+} buffering (Borst and Sakmann, 1998; Cuttle et al., 1998; Hori and Takahashi, 2009). In MLIs, enhancement of spike-evoked Ca^{2+} entry following subthreshold depolarization could reflect a comparable Ca^{2+}-dependent facilitation of VSCC activity, as MLIs express NCS-1 at presynaptic sites of release (Jinno, Jeromin, Roder, and Kosaka, 2002; Jinno, Jeromin, and Kosaka, 2004). It remains possible that facilitation of action potential-evoked Ca^{2+} entry does not depend directly on the Ca^{2+} elevation evoked by the subthreshold depolarization. Alternatively, because spike-evoked Ca^{2+} influx in presynaptic terminals is, in part, controlled by the amplitude and duration of the action potential waveform (Bischofberger et al., 2002; Geiger

and Jonas, 2000), facilitation of spike-evoked Ca^{2+} entry following subthreshold depolarization may reflect an alteration of the underlying action potential. Prolonged subthreshold somatic depolarization inactivates axonal Kv1 potassium channels in L5 pyramidal cells of visual cortex, leading to spike broadening (Kole et al., 2007), which should in turn enhance Ca^{2+} entry (Geiger and Jonas, 2000). However, potassium channel inactivation is not expected to be EGTA-sensitive or depend on VSCCs, arguing against this possibility.

Somatic depolarization and enhancement of release

Presynaptic receptor-mediated depolarization of calyceal nerve terminals elicits VSCC Ca^{2+} elevation and strengthening of release (Awatramani et al., 2005; Turecek and Trussell, 2001). Our results extend this finding; subthreshold excitatory potentials need not only be elicited on or near terminals to enhance release. Depolarizing potentials evoked in the dendrites or soma spread through the axon, opening VSCCs, elevating Ca^{2+} at presynaptic specializations, and thereby increasing the likelihood of transmission. Small Ca^{2+} transients increase the probability of fusion by increasing microdomain Ca^{2+} (Felmy, Neher, and Schneggenburger, 2003; Müller, Felmy, and Schneggenburger, 2008), recruiting or sensitizing vesicles through Ca^{2+} binding by a high-affinity sensor distinct from the exocytosis trigger (Atluri and Regehr, 1996; Tang, Schlumpberger, Kim, Lueker, and Zucker, 2000), and saturating endogenous Ca^{2+} buffers (Felmy et al., 2003; Müller et al., 2008). If these mechanisms are mediated by residual Ca^{2+} following action potential firing, then they may also be triggered by Ca^{2+} influx during subthreshold depolarization (Hori and Takahashi, 2009). Given that release probability is steeply dependent on the intracellular $[Ca^{2+}]$ (Bollmann et al., 2000; Schneggenburger and Neher, 2000), enhancement of spike-evoked Ca^{2+} entry will also strengthen transmission (Borst and Sakmann, 1998; Cuttle et al.,

1998; Geiger and Jonas, 2000; Hori and Takahashi, 2009) unless the release process is saturated. If this occurs in MLIs, it may explain why high release probability synapses have a diminished capacity for release-strengthening induced by subthreshold depolarization.

We show that axonal VSCC-mediated Ca^{2+} entry elicited during presynaptic depolarization is sufficient to evoke asynchronous release in MLIs. Ca^{2+}-induced asynchronous fusion has a relatively high sensitivity to intracellular [Ca^{2+}], with an elevation to as little as 1 μM triggering release (Bollmann et al., 2000; Schneggenburger and Neher, 2000). If the Ca^{2+} sensor for asynchronous exocytosis at MLIs has a similar sensitivity, then the intracellular [Ca^{2+}] reached at MLI varicosities may be much higher than depolarization-evoked Ca^{2+} elevation in the calyx (100 nM; Awatramani et al., 2005). The supra-linear Ca^{2+}cooperativity for exocytosis (Bollmann et al., 2000; Heidelberger, Heinemann, Neher, and Matthews, 1994; Schneggenburger and Neher, 2000) might suggest a greater amount of spike-evoked release enhancement following presynaptic depolarization and Ca^{2+} entry than we observed. However, asynchronous transmission can deplete the pool of release-ready vesicles, diminishing availability for phasic transmission (Lu and Trussell, 2000; Otsu et al., 2004). The resulting short-term depression of release can develop concomitantly with facilitation, one effect masking the other (Dittman et al., 2000; Müller et al., 2010). In this way, the capacity for depolarization-evoked strengthening of transmission in MLIs is limited by the superimposition of Ca^{2+}-dependent depression mediated by vesicle pool depletion. Though IPSC amplitudes were unchanged by subthreshold depolarization in EGTA, it may be that release enhancement was merely balanced by depression rather than fully blocked. EGTA only partially diminished depolarization-induced Ca^{2+} elevation suggesting that the Ca^{2+}-dependent effects on release persisted in this condition. The expression of facilitation and depression will depend on the relative Ca^{2+} sensitivity of each mechanism.

As implied in our burst-firing experiment, the capacity for release-strengthening by subthreshold depolarization smay be strongly limited by depletion. Non-homogenous pools of vesicles may populate presynaptic sites at MLIs, as they do at the calyx of Held (Wu and Borst, 1999). Subthreshold depolarization may help recruit more reluctant vesicles, distinguished by their relative Ca^{2+} sensitivity and/or distance from VSCCs, to participate in release during subsequent action potential-evoked transmission. Bulk Ca^{2+} elevation evoked by repetitive firing may also recruit these vesicles, depleting their availability and thereby decreasing the capacity for subthreshold depolarization induced enhancement of release. That is, multiplicative non-linear processes are competing for overlapping vesicle pools to determine the expression of short-term plasticity. We expect that any reduction in the vesicle pool(s), mediated by preceding sub- or suprathreshold activity, would diminish enhancement of release induced by subthreshold depolarization.

Functional implications

Subthreshold depolarization-induced regulation of spike-evoked release is clearly important in a number of cell types, though the mechanisms underlying the regulation may vary across brain regions (Alle and Geiger, 2006; Christie and Jahr, 2008, 2009; Kole et al., 2007; Scott et al., 2008; Shu et al., 2006). In MLIs, the phenomenon appears to be entirely dependent on axonal Ca^{2+}, as observed for other forms of release-strengthening (Zucker and Regehr, 2002). In contrast, at hippocampal mossy fiber synapses, it may be that the Ca^{2+}-dependence is restricted to proximal portions of the axon, whereas at more distal sites other mechanisms of strengthening are involved (Scott et al., 2008), such as potassium channel inactivation (Geiger and Jonas, 2000; Kole et al., 2007). One clear difference between these two cell types is axonal length, mossy fibers being much longer than MLI axons. Even in MLIs, the increases in axonal Ca^{2+} are, on average, larger in proximal than in distal portions

of the axon, as expected from cable properties (Christie and Jahr, 2008). However, there was no correlation between the depolarization-induced enhancement of release and distance between the somata of synaptically connected pairs (r^2 = 0.06, p = 0.23; n = 27), though this comparison is likely compromised by the inaccuracy of this measurement in predicting axonal length. The present results suggest that Ca^{2+}-dependent plasticity induced by somatic depolarization will affect the gain of most synapses in short axon cells and at least proximal synapses in other cell types. However, it is likely that depolarization-induced plasticity does not simply monotonically decay with distance from the soma given the amount of variance we observed in our Ca^{2+} imaging and paired recording experiments. The control of transmitter release by subthreshold synaptic input that precedes action potential initiation adds a new dimension to synaptic signaling and requires consideration when analyzing information transfer across synapses.

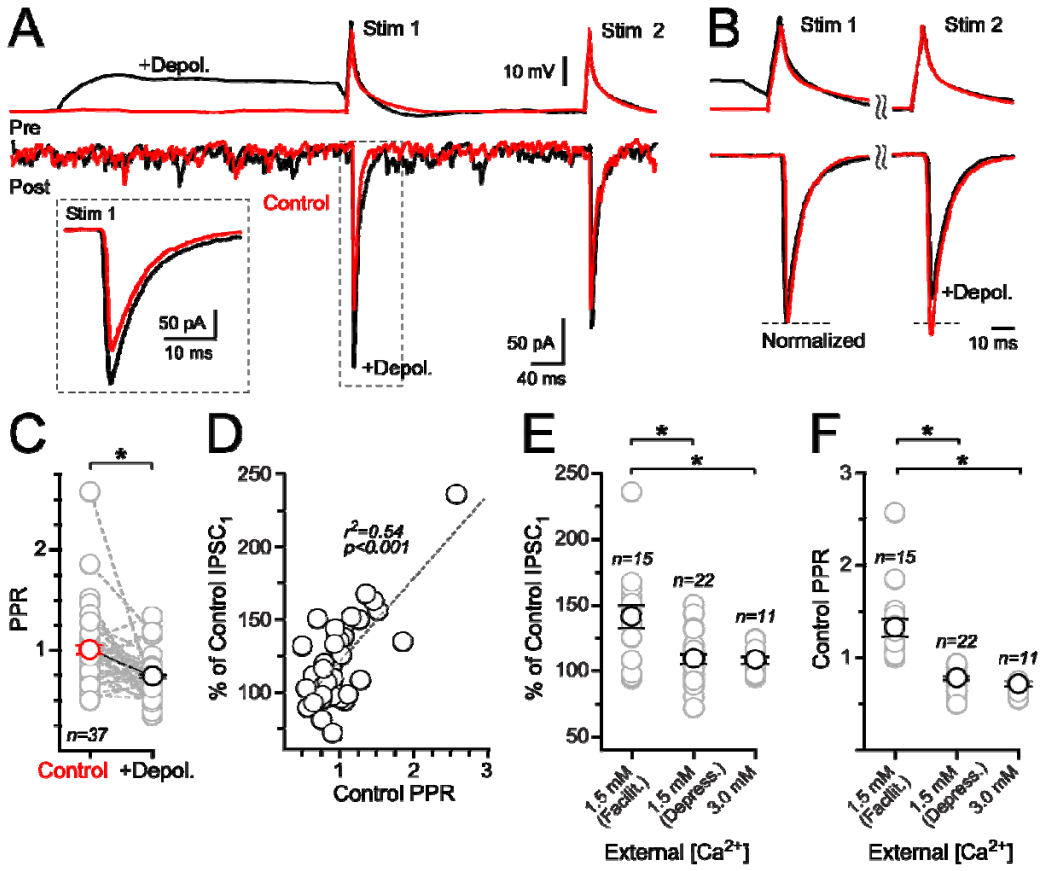

Figure 1.1

Subthreshold somatic depolarization enhances spike-evoked release in MLIs

(A) In a MLI paired recording, action potentials in the presynaptic neuron evoked $GABA_A$R-mediated IPSCs in the postsynaptic neuron. Subthreshold somatic depolarization (300 ms) elicited prior to spiking enhanced release. Control action potential responses are in red and test responses preceded by subthreshold depolarization are in black. An amplified view of the first IPSC is shown in the inset. (B) Paired-pulse IPSCs from the same neuron normalized to the peak of the first response. (C) Summary data show that the PPR decreases with somatic depolarization of the presynaptic neuron. A significant difference (paired t-test, $p < 0.05$) between groups is indicated by asterisk with mean values ± SEM. (D) Linear regression analysis indicates that release enhancement elicited by subthreshold depolarization

was correlated with the basal PPR. (E and F) Differences in release enhancement for facilitating and depressing responses measured in 1.5 and 3.0 mM extracellular Ca^{2+}. ANOVA analysis with post-hoc Tukey's multiple comparison tests indicated significance ($p < 0.05$) with mean values plotted ± SEM. For clarity, spontaneous IPSCs were blanked prior to averaging in A (inset) and B.

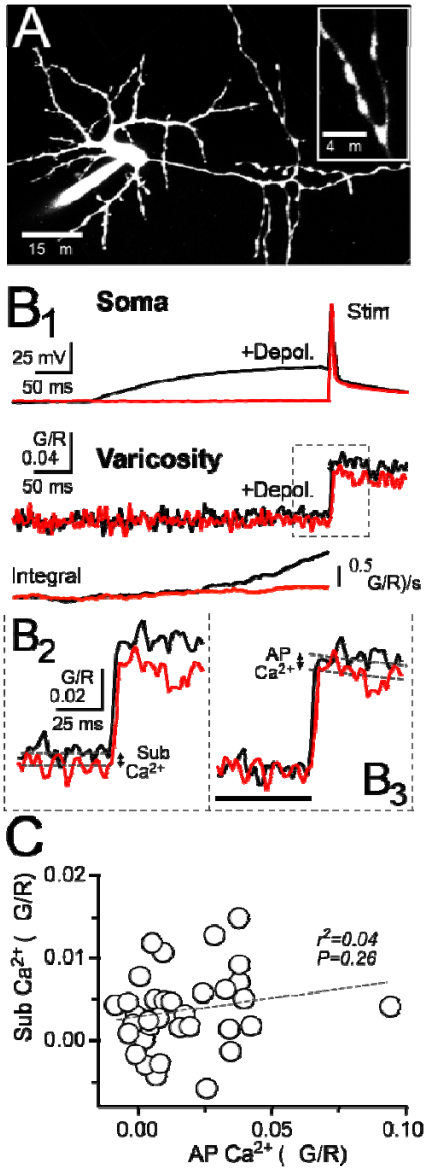

Figure 1.2

Subthreshold somatic depolarization evokes and enhances axonal Ca^{2+} entry

(A) Two-photon fluorescence image of a representative MLI filled via patch pipette with Alexa 594 (13 μM) and Fluo-5F (200 μM). On the right, a higher-magnification view shows axon varicosities. (B_1) Somatic current injection elicited control action potential-evoked responses (red) and test spikes paired with 300 ms subthreshold depolarizations (black).

Shown below are the resulting Ca^{2+} transients recorded in an axon varicosity. At the bottom, integration of the Ca^{2+} signals accentuates the difference between control and depolarized responses prior to spike firing. (B_2) Amplified view of Ca^{2+} transients with dashed lines (100 ms epoch average) demarcating the amplitude of the Ca^{2+} response evoked by subthreshold depolarization. (B_3) Action potential-evoked Ca^{2+} transients baselined prior to spike firing (black bar) isolated depolarization-dependent facilitation of the spike-evoked Ca^{2+} transient. Exponential fits to the spike-elicited transients were used to determine peak amplitudes. (C) Comparison of depolarization-evoked Ca^{2+} elevation and facilitation of action potential-elicited Ca^{2+} entry. Line fit of the linear regression is indicated by the dashed line.

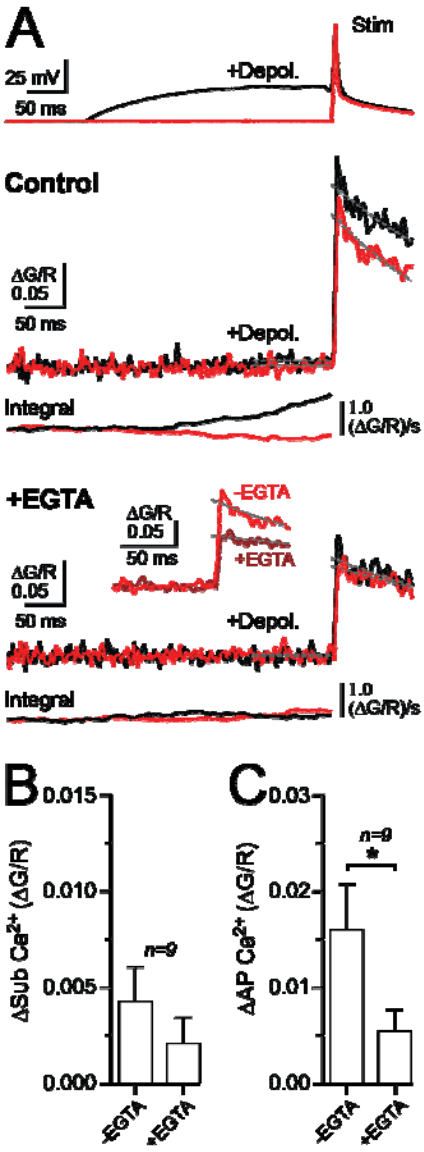

Figure 1.3

Subthreshold depolarization-dependent Ca^{2+} signaling is EGTA-sensitive

(A) Somatic recording of an action potential (red) and an action potential preceded by a 300 ms subthreshold depolarization (black). The resulting Ca^{2+} transients in an axon varicosity are shown below in control and following EGTA-AM application (10-20 μM; >10 min). Integrals of the Ca^{2+} responses are provided for each condition. The inset shows a

comparison of action potential-evoked responses, elicited without preceding subthreshold depolarization, in control and with EGTA. Dashed lines indicate the response amplitude prior to spiking (100 ms epoch) and the exponential fits of action potential-evoked Ca^{2+} transients used to determine peak amplitudes. (B) The effect of EGTA on Ca^{2+} entry evoked by subthreshold depolarization. (C) EGTA inhibits facilitation of spike-evoked Ca^{2+} entry caused by subthreshold depolarization. Mean values are presented with error bars (+ SEM); asterisks denote significance (paired t-test, $p < 0.05$).

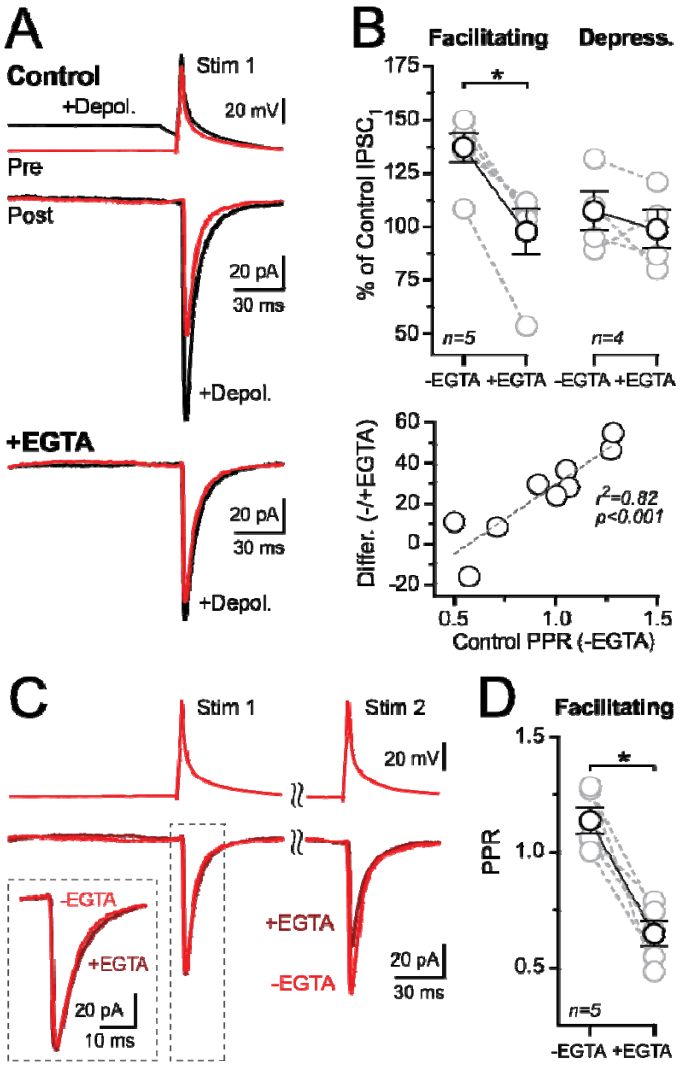

Figure 1.4

EGTA inhibits enhancement of release elicited by subthreshold depolarization

(A) Action potential-evoked IPSCs (red) recorded from pairs of connected MLIs in control and following EGTA-AM application. In alternating trials, action potentials were preceded by a 300 ms subthreshold depolarization (black). (B) Top summary graph shows that EGTA eliminates release strengthening caused by subthreshold depolarization in facilitating cell pairs. Release-strengthening was not apparent in cell pairs that depressed in basal conditions. In the bottom graph, linear regression analysis plots the difference between the percentage

change in EGTA and in control relative to the basal PPR. (C) The effect of EGTA on paired-pulse responses from trials without preceding subthreshold depolarization. Amplified view of the first IPSC is shown on the inset. (D) EGTA altered paired-pulse responses in cell pairs that facilitated in basal conditions. Data are plotted as mean values with ± SEM and asterisks denote significance (paired t-test, $p < 0.05$). Spontaneous IPSCs were blanked prior to averaging in A and C.

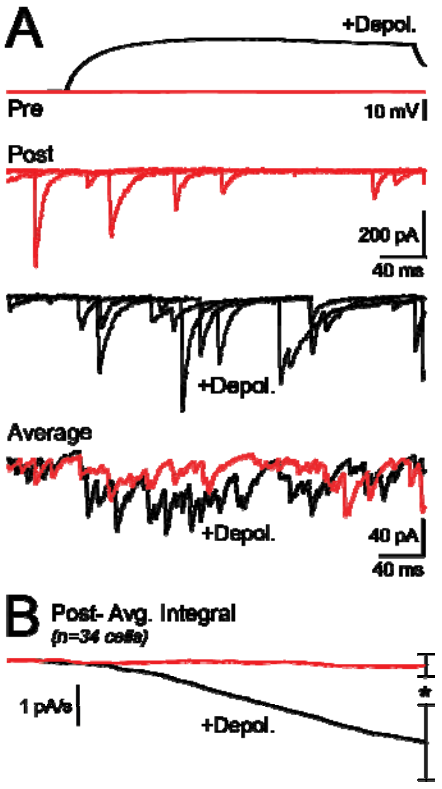

Figure 1.5

Subthreshold depolarization evokes asynchronous release

(A) Paired recording of MLIs show spontaneous IPSCs in unstimulated control responses (red) and recruitment of asynchronous events with a 300 ms presynaptic subthreshold depolarization (black). Three individual sweeps from the postsynaptic neuron are shown superimposed for each condition with the average response (27 and 28 sweeps, control and depolarized, respectively) at the bottom. (B) The average charge integration of the postsynaptic response across all cell recordings (± SEM). Asterisk denotes significance (paired t-test, $p < 0.05$).

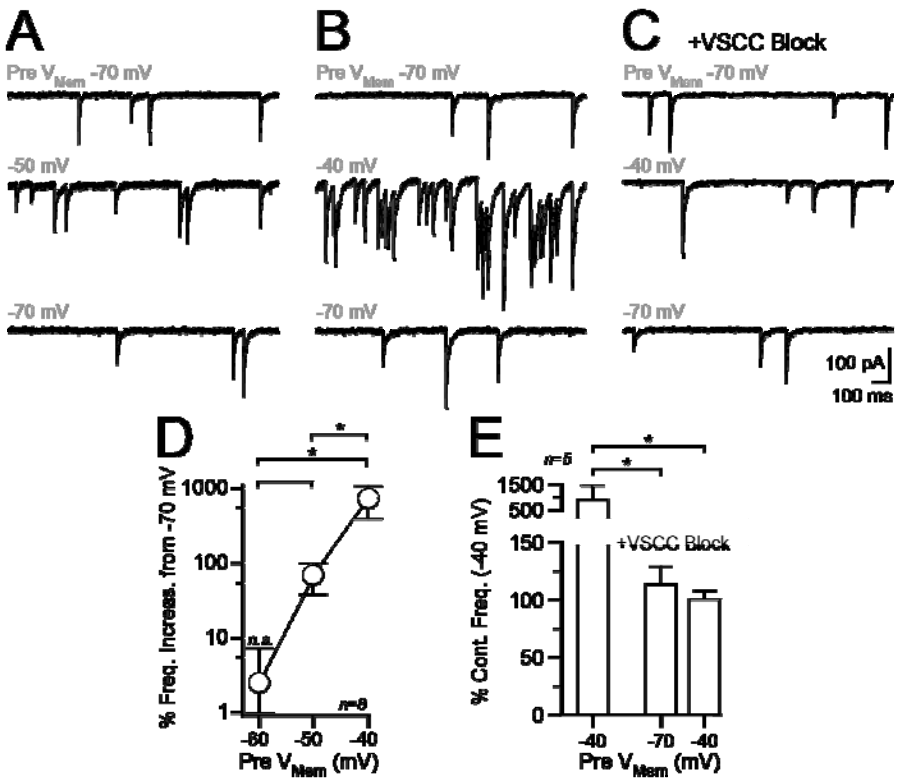

Figure 1.6

Depolarization-dependent asynchronous release is triggered by VSCCs

(A and B) Paired recording from MLIs in TTX with representative sweeps from the postsynaptic neuron showing recruitment of asynchronous IPSCs with presynaptic depolarization. The presynaptic holding potential is indicated in gray above each sweep. Responses were recorded in 3 mM extracellular Ca^{2+} to enhance release. (C) In the same cell, IPSC frequency is unaltered by presynaptic depolarization after VSCC block (100 μM Cd^{2+} and Ni^{2+}). (D) Asynchronous IPSC frequency depends on the presynaptic holding potential. Mean values are plotted with error bars ± SEM. Asterisks denote significant differences ($p < 0.05$) between groups tests following ANOVA analysis (Tukey's multiple comparison test). (E) Block of VSCCs eliminates the depolarization-dependent increase in asynchronous transmission. Mean values + SEM are shown with significance (asterisks $p < 0.05$) determined by ANOVA analysis.

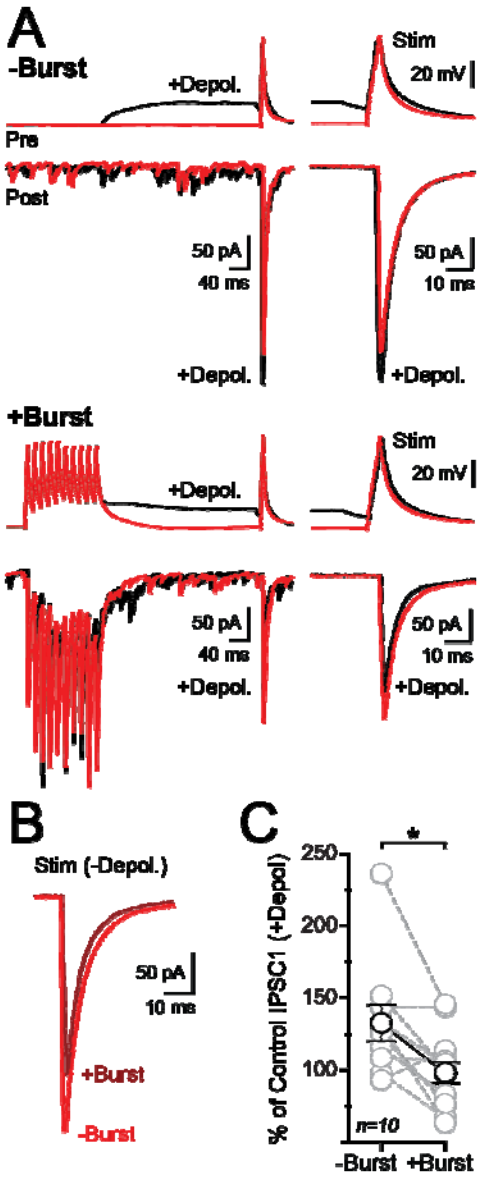

Figure 1.7

Burst firing reduces the capacity for release enhancement caused by depolarization

(A) In a recording from connected MLIs, high-frequency bursts of action potentials (10 spikes, 60 Hz) preceded a 300 ms subthreshold stimulation and test spikes in interleaved trials. Amplified views on the right show release enhancement caused by subthreshold depolarization and weakening of transmission when subthreshold excitation was paired with

burst firing. (B) The effect of burst firing on the first IPSC in control trials without subthreshold stimulation is shown. (C) Burst firing eliminated release strengthening induced by subthreshold depolarization. Mean values are illustrated ± SEM with significance denoted by an asterisk (paired t-test, $p < 0.05$). For amplified views (A and B) spontaneous events were blanked prior to averaging.

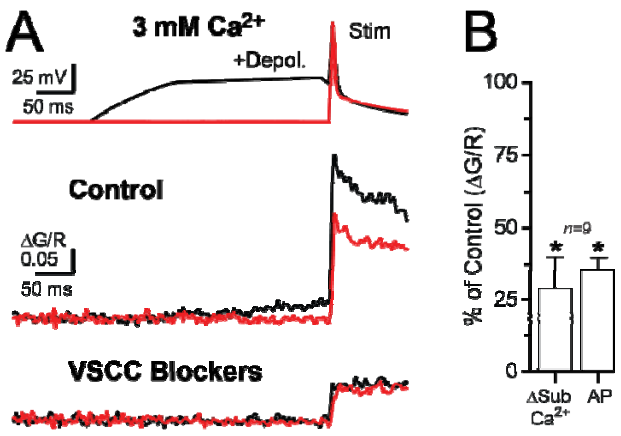

Supplemental Figure 1.1

Subthreshold depolarization evokes and enhances Ca^{2+} entry through VSCCs

(A) An action potential with (black) and without (red) a preceding subthreshold depolarization (300 ms) recorded in the soma. Shown below are the resulting Ca^{2+} transients recorded in an axon varicosity (3 mM extracellular Ca^{2+}) in control and following inhibition with a combination of VSCC blockers (ω-conotoxin MVIIC 1 μM, SNX 0.3 μM, nimodipine 20 μM, and mibefradil 10 μM). (B) Inhibition of axonal Ca^{2+} transients by VSCC blockers. Mean values are presented with error bars (+ SEM); asterisks denote that the reductions from control responses were significant (paired t-test, $p < 0.05$).

CHAPTER 2.

ASYMMETRIC STRUCTURAL PLASTICITY AT A HIPPOCAMPAL SYNAPSE

Delia N. Chiu[1, 2], Brett C. Carter[1], and Craig E. Jahr[1]

[1]Vollum Institute, Oregon Health and Science University

[2]Neuroscience Graduate Program, Oregon Health and Science University

Portland, OR USA

Foreword

I did preliminary experiments for this chapter over the course of two years, during which I received many ideas and suggestions from labmates and my Thesis Advisory Committee. Once I learned the technique of *in utero* electroporation, I was helped greatly by Dr. Brett Carter, who assisted in both data collection and analysis. He performed the CA1 spine experiments and roughly half of the CA3 varicosity experiments. I analyzed the data primarily with functions he wrote in IGOR. All figures were assembled by me.

Abstract

Structural plasticity has been observed in dendritic spines, and is believed to play a role in the maintenance of functional plasticity. It is unclear, however, whether presynaptic structures also display structural plasticity. Given the ultrastructural evidence that dimensions of pre- and postsynaptic structures are correlated, and increase with synaptic strength, we hypothesized that increases in spine volume caused by repetitive glutamate uncaging should be accompanied by increases in volume of their apposing presynaptic varicosities. In acute slices of rat hippocampus, we observed structural plasticity of dendritic spines following a standard glutamate uncaging protocol. These changes persisted for two hours. In contrast, no morphological changes were seen in CA3 axonal varicosities on this time scale.

Introduction

Synaptic plasticity allows synapses to undergo experience-dependent changes in strength. Recent studies have revealed an anatomical component or correlate of these changes. This structural plasticity, as observed in cortical and hippocampal pyramidal neuron dendritic spines, has many of the hallmarks of synaptic plasticity.

It was not until recently that the technology was available to definitively link structural changes with the development of functional plasticity. Matsuzaki and colleagues demonstrated that spine morphology was altered by stimuli that induced potentiation of the postsynaptic response in a subset (30%) of spines. This structural plasticity had many features in common with functional LTP, in that it was NMDA receptor-, calmodulin-, and CAMKII-dependent (Matsuzaki, Honkura, Ellis-Davies, and Kasai, 2004).

Experiments addressing consequences of both functional and structural plasticity on presynaptic morphology, however, have been lacking (Becker, Wierenga, Fonseca, Bonhoeffer, and Nägerl, 2008). There are several reasons that postsynaptic structural plasticity suggests the existence of presynaptic structural plasticity.

First, there are a number of studies that show coordination in the number and size of pre- and postsynaptic structures (Bourne and Harris, 2011). Second, active zone size correlates with postsynaptic density (PSD) size (Lisman and Harris, 1993; Meyer, Bonhoeffer, and Scheuss, 2014; Schikorski and Stevens, 1997), and active zone size correlates with bouton size (Schikorski and Stevens, 1997).

Third, pre- and postsynaptic membranes are physically linked by cell adhesion molecules (CAMs) including N-cadherin (Takeichi, 1988), neurexins-neuroligins (Ichtchenko et al., 1995), EphA-ephrinA (Hruska and Dalva, 2012), EphB-ephrinB signaling (Dalva, McClelland, and Kayser, 2007) and many others (see Yang, Hou, Jiang, and Zhang, 2014).

Finally, time lapse imaging of pre- and postsynaptically expressed proteins has provided evidence synapses don't separate, even during periods of overall motility (Fisher-Lavie and Ziv, 2013; Umeda, Ebihara, and Okabe, 2005). Taken together with the evidence that spine volume can increase dramatically after potentiation, this raises the question of whether boutons undergo an analogous change in morphology. To address this question, we imaged axonal varicosities of eGFP-expressing CA3 neurons in acute slice before and after LTP-inducing stimuli. We do not find evidence for structural changes akin to those seen in dendritic spines in these structures.

Materials and Methods

In utero electroporation

To enable visualization of cell morphology in acute slices, a subset of hippocampal neurons was transfected with a pCAG-e*GFP* DNA plasmid (kind gift from Dr. Tianyi Mao) via *in utero* electroporation on E17-18 rat pups, in accordance with Oregon Health and Science University Institutional Animal Care and Use Committee (OHSU IACUC). Timed pregnant Sprague Dawley dams (Charles River, MA) were anesthetized with isoflurane. DNA plasmid (0.4 μg/μL in deionized water, with Fast Green for visualization) was injected into the lateral ventricle of each embryo using a fine-tipped glass pipette. Following injection, a series of voltage pulses (5 x 50 ms, 50 mV) was delivered to each embryo using external paddles.

After surgery, dams recovered for ~ 1 hr in a cage with warmed bedding and were monitored for signs of distress before being returned to animal housing facility. Dams were administered Meloxicam (2 mg/kg) before surgery and once a day for two days post-operatively.

Slice preparation

Transverse cortical slices (300 μm) were prepared from rats of either sex (PND20-25) according to protocols approved by the OHSU IACUC. Animals were deeply anesthetized with isoflurane and decapitated. Brains were quickly removed and placed in ice-cold solution containing the following (in mM): 87 NaCl, 2.5 KCl, 7.0 $MgCl_2$, 1.25 NaH_2PO_4, 25 $NaHCO_3$, 25 glucose, 75 sucrose (saturated with 95% O_2/5% CO_2). The slices were cut using a Leica VT1200S vibrating blade microtome (Leica Instruments, Nussloch, Germany) and transferred to a 36°C recovery chamber with artificial cerebrospinal fluid

(ACSF) containing (in mM): 119 NaCl, 2.5 KCl, 2.0 $CaCl_2$, 1.0 $MgCl_2$, 1.0 NaH_2PO_4, 26.2 $NaHCO_3$, 11 glucose, 3 Na-pyruvate, and 1.3 Na-ascorbate (saturated with 95% O_2/5% CO_2). After 30 min at 36°C slices were maintained at room temperature for 1-5 hours before use.

Slices were superfused with a modified version of the above ACSF, containing 3.3 mM $CaCl_2$ and 0.05 mM $MgCl_2$, as well as 0.5 μM tetrodotoxin (TTX), 50 μM picrotoxin, and 2.5 mM MNI glutamate. For blinded experiments, an aliquot containing either external solution or D-AP5 (final concentration 50 μM) was added to the ACSF prior to experimental begin each day. This solution was re-circulated using a peristaltic pump. Experiments were done at room temperature.

Imaging

Imaging and uncaging were performed on a custom-built two-photon laser scanning microscope using an Olympus (Melville, NY) upright microscope and objective (60×, 1.0 NA) and two Chameleon Ti:Sapphire lasers (Coherent, Santa Clara, CA). Lasers were tuned to 955 or 980 for eGFP excitation and 725 nm for uncaging. Green and red fluorescence was collected by photomultipliers (H8224P-40 or H10770PA-40, Hamamatsu, Hamamatsu City, Japan) in epi- and transfluorescence pathways using a 565 dichroic mirror and 525/50 and 620/60 band-pass filters (Chroma Technology, Brattleboro, VT). Images were acquired using custom software (T.A. Pologruto and B.L. Sabatini) written in MATLAB (MathWorks, Natick, MA).

Glutamate uncaging

Uncaging pulses (0.6 ms) were delivered at 1 Hz for 60 seconds (Matsuzaki et al., 2004). Uncaging laser power was set according to depth, such that a single pulse resulted in

~40% bleaching of Alexa 594 (data not shown).

Image analysis

Two to eight regions of interest (ROIs) were chosen at the beginning of an experiment and their x,y,z-coordinates recorded. Image stacks were acquired at each position in 15-minute intervals, including at least two time points prior to uncaging protocol, and consisted of 5-10 frame scans (0.8 μM z-step).

A z-projection of the sum of each stack was used for post hoc analysis. Fluorescence is proportional to volume (Svoboda, 2004); thus, ROI fluorescence at each time point was measured and background fluorescence, equal to the average background pixel value times the number of pixels in the ROI, was subtracted. ROI fluorescence for time points after uncaging was normalized to the average of 2-3 baseline values.

Owing to the inconsistency with which we were able to follow axons to CA1, our data include boutons from closer to the CA2 or CA3 region of stratum radiatum, as in Meyer et al. (2014). The experiments in Figure 2.3 demonstrate that structural plasticity in spines of CA3 apical dendrites is similar to that observed in CA1 spines. This result justifies our decision to include varicosities within CA3 in our results. As no differences were observed between varicosities ~100 μm from CA3 cell bodies and those up to 200 μm distant, data were pooled.

Statistical analysis

Data were analyzed using both custom-written regimes in IGOR (WaveMetrics, Lake Oswego, OR) and Excel (Microsoft, Seattle, WA). Reported values are expressed as mean ± SEM. Student's t-test (paired, two-tailed) was used to determine statistical significance.

Differences were considered statistically significant with α values of $p < 0.05$. In figures, asterisks denote statistical significance.

Results

Spine structural plasticity is induced by glutamate uncaging in acute slice

eGFP was expressed in a subset of hippocampal pyramidal neurons by in utero electroporation (Fig. 2.1). In control experiments, MNI glutamate was uncaged on spines of eGFP-expressing CA1 neurons in acute slices using a protocol known to induce functional and structural plasticity in spines in organotypic slice culture (Matsuzaki et al., 2004) (Fig. 2.2A). After uncaging, spine fluorescence increased rapidly, to a peak of 201.1% ± 30.0% one minute after uncaging, and then decreased. In 12 of 29 spines tested, spine fluorescence at 90 minutes after uncaging was not different from baseline (± one standard deviation of baseline values). However, across all spines, average spine fluorescence remained elevated compared to baseline for 90 minutes, the duration of observation (134 ± 9.9%; n = 29, p = 0.0003; Fig. 2.2B).

Next, spines of eGFP-expressing CA3 neurons were tested with the same uncaging protocol (Fig. 2.3A). Spines increased in volume in a manner similar to CA1 spines, displaying both a transient and a persistent increase (164.7 ±17.5% at 90 min; n = 5, p = 0.008) (Fig. 2.3B). The changes in volume did not occur in experiments in which D-AP5 (50 μM) was present (68.7 ± 9.9% at 90 min; n = 11) (Fig. 2.3C), indicating that structural plasticity in CA3 spines, like those in CA1, is NMDA receptor-dependent.

Morphological changes are not observed in CA3 axons after glutamate uncaging

Having observed postsynaptic structural plasticity of the spines of eGFP-expressing CA1 and CA3 pyramidal neurons in acute slice, we turned our attention to the presynaptic morphology. The same plasticity-inducing uncaging protocol was used on CA3 axonal varicosities (Fig. 2.4A). We reasoned that structural plasticity in varicosities would be

NMDAR-dependent, as both functional and structural postsynaptic plasticity have been shown to be. While we were not simultaneously monitoring the postsynaptic partner to the varicosity, we assumed that, because of the close proximity between spine and varicosity, NMDARs on the postsynaptic spine were activated and that spine plasticity was induced. To control for changes in varicosity size that are independent of the induction protocol, all experiments were performed and analyzed in an AP5-blind manner (Fig. 2.4B).

Following uncaging, varicosity size did not increase either transiently or during subsequent observations in either experimental group (Fig. 2.4B, C). With D-AP5 present, no increase in fluorescence was measured, as might be expected; fluorescence was 86.6 ± 6.8% of baseline at the first time point after uncaging (15 minutes) and 99.9 ± 4.4% at 120 minutes (n = 65). In ACSF only, however, fluorescence also did not increase after uncaging. In fact, we measured a decrease in fluorescence compared to baseline over time (88.7 ± 1.7% at 15 minutes and 79.9 ±2.5% at 120 minutes; n = 61).

We conclude that, unlike CA1 and CA3 dendritic spines, CA3 axon varicosities do not undergo an increase in size within the first two hours after an LTP-induction protocol (Fig. 2.4 D).

Discussion

Spines in acute slice display structural plasticity

We find that CA1 dendritic spines undergo structural plasticity in acute brain slice. The time course and magnitude of the persistent changes in volume following a potentiating glutamate uncaging protocol are in agreement with published results from transfected cells in organotypic slice culture. To our knowledge, this is the first demonstration of structural plasticity in CA3 spines.

Axons do not change on the timescale of spines

Postsynaptic structural plasticity occurs on the same time scale as functional plasticity (Matsuzaki et al., 2004). We find no evidence, however, for presynaptic changes over the same time course. This correlates with the majority opinion that at least early LTP at these synapses results from an increase in postsynaptic expression of AMPA receptors without changes in presynaptic function (Kessels and Malinow, 2009). We also find that the presence of D-AP5 during the induction protocol had no effect on the outcome, indicating that any variation in varicosity size in control conditions cannot be ascribed to NMDAR-dependent plasticity.

An alternative explanation for our findings is that the duration of these experiments was not sufficient to measure changes in axon morphology. A recent study by Bonhoeffer and colleagues (Meyer, Bonhoeffer, and Scheuss, 2014) provides evidence that boutons, like spines, swell after an LTP-inducing protocol. The increase in bouton volume was significant beginning at 120 minutes, supporting the idea that presynaptic structural plasticity develops more slowly than postsynaptic and functional plasticity. However, our data do not demonstrate an increase in volume even at 120 minutes after uncaging.

One possible explanation for the discrepancy between our results and these recent findings (Meyer, Bonhoeffer, and Scheuss, 2014) is the use of acute versus organotypic slice. Although our ability to induce structural plasticity in spines suggests that the phenomenon is not exclusive to cells in organotypic slices, given our negative result, further experiments are necessary. We are interested in testing cultured slices to see if this methodological difference affects the ability to induce or observe structural plasticity in axons.

Other groups have noted that structural plasticity in spines is not induced in all spines tested, but Meyer and colleagues observed growth in 7 of 10 boutons tested. This is the inverse of the case in CA1 spines, where only 30% displayed persistent growth (Matsuzaki et al., 2004). This result could indicate that bouton plasticity is induced more easily than spine structural plasticity, or that structural plasticity in boutons can occur independently of structural plasticity in postsynaptic partner. Both interpretations contrast starkly with our findings, however; only two of 61 varicosities tested were larger than baseline by more than one standard deviation 120 minutes after uncaging.

It remains untested whether NMDARs play a role in presynaptic structural plasticity. We designed our experiments based on the hypothesis that NMDARs are required, as they have been shown to be in spine structural plasticity. The authors of the recent paper (Meyer, Bonhoeffer, and Scheuss, 2014) do not test the role of NMDARs, however, and, although pre- and postsynaptic morphological changes are correlated, it is possible that the phenomenon they observe has a different mechanism than the structural plasticity seen in spines, and which we set out to investigate.

Still, our study is based on two key assumptions. The first is that the varicosities tested were functional boutons. Previous work has confirmed that visually identified varicosities displayed hallmarks of sites of release: action potential-evoked calcium transients mediated by voltage-sensitive calcium channels that are much larger than those seen in non-

varicose regions of axon. In a set of preliminary experiments, CA3 neurons were filled with calcium indicator through the patch pipette and line scans across varicosities revealed AP-evoked calcium transients. Having a functional reporter, such as a genetically encoded calcium fluorophore, might be useful for future experiments, so that there is less uncertainty about whether varicosities are sites of release.

The other major assumption is the presence of a postsynaptic spine at the varicosity of interest. As the goal is to observe presynaptic structures during and after development of postsynaptic structural plasticity, experiments should be done to confirm, either in real time or with post hoc analysis, whether structural plasticity did, in fact, take place. Though Matsuzaki et al. (2004) demonstrated a robust form of plasticity in spines, they noted that uncaging did not lead to plasticity in all or even most spines tested. Thus, one shortcoming of our study is that we do not know how many spines that were synaptically paired with the varicosities we targeted actually underwent structural plasticity.

Literature on structural plasticity in CA1 dendritic spines motivated this work; we therefore wanted to target varicosities in stratum radiatum of CA1, which is 200-1000 μm distant from CA3 somata. Though hippocampus is a laminar structure, CA3 axons do not have a laminar organization, making it impossible to predict their paths, or, to our knowledge, prepare acute slices in such a way as to dramatically increase the likelihood of including both soma and axon in one slice.

Future experiments

One of the parameters that might be further investigated is the method of acute slice preparation. Kristen Harris's lab has shown that ice-cold solution causes retraction of spines in hippocampal slices (Bourne, Kirov, Sorra, and Harris, 2007). Recovery in warmed solution reverses the effect, but it is unclear whether this could be a form of potentiation that could

occlude either functional or structural plasticity. Though we observed structural plasticity in spines using our method of slice preparation, it is possible that slices prepared without cooling and re-warming respond differently. Along those lines, cells in organotypic slice culture, which have been used in all other studies of uncaging-evoked structural plasticity in hippocampus, have had days, not hours, to recover from exposure to ice-cold solution than cells in acute slice.

One question that the present work does not address is whether presynaptic activity could be required for presynaptic structural changes. That is, even though glutamate uncaging can bypass presynaptic activation and cause plasticity in spines, might firing be necessary for presynaptic structural plasticity? Morphological changes in the spine depend on cytoskeletal remodeling, cues for which are downstream of calcium (Matsuzaki et al., 2004). If presynaptic structural plasticity also depends on an increase in calcium, it will not occur under the conditions of our experiment. To test this, we could pair stimulation of axons of interest with glutamate uncaging.

Acknowledgments

The pCAG-e*GFP* DNA plasmid used in this study was a generous gift from Dr. Tianyi Mao. We would also like to thank Dr. Gail Mandel and Dr. Paul Brehm for providing the space and equipment necessary to carry out *in utero* electroporation, and Dr. Wendy Wu for teaching us the technique. Members of the Zhong Lab provided reagents for and instruction in the steps of DNA plasmid preparation.

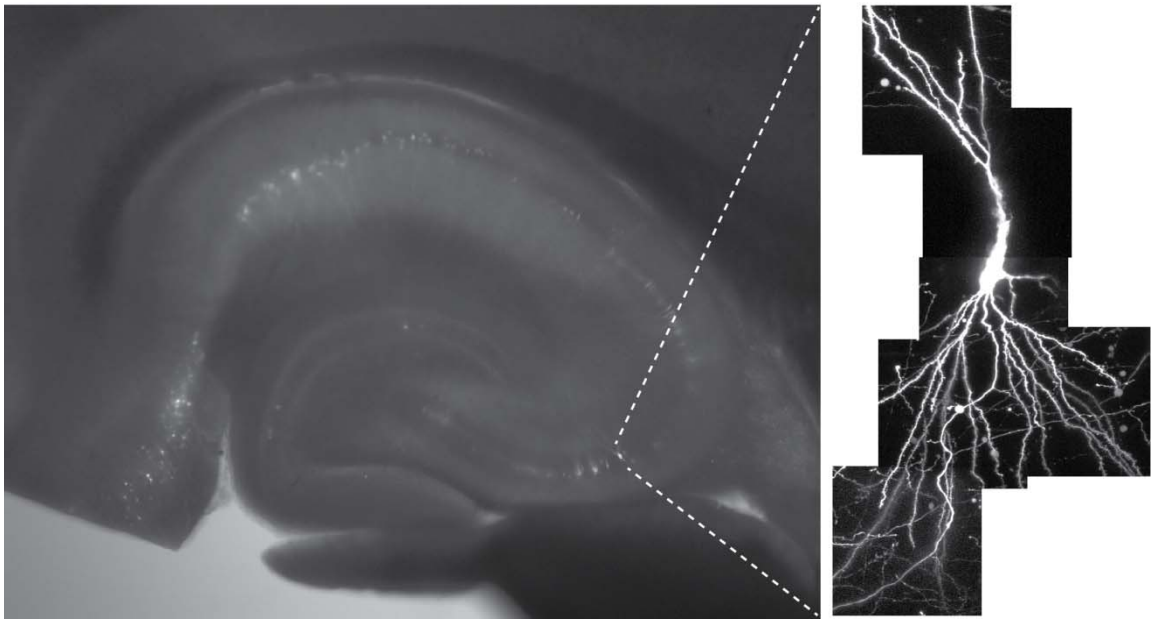

Figure 2.1

Expression of eGFP in a subset of hippocampal pyramidal neurons following *in utero* electroporation.

Transverse cortical slice from P20 rat, electroporated at E17. Image of merged brightfield illumination and eGFP fluorescence at low magnification shows expression of eGFP by hippocampal pyramidal neurons. At right, two-photon fluorescence image of a representative CA3 pyramidal neuron expressing eGFP.

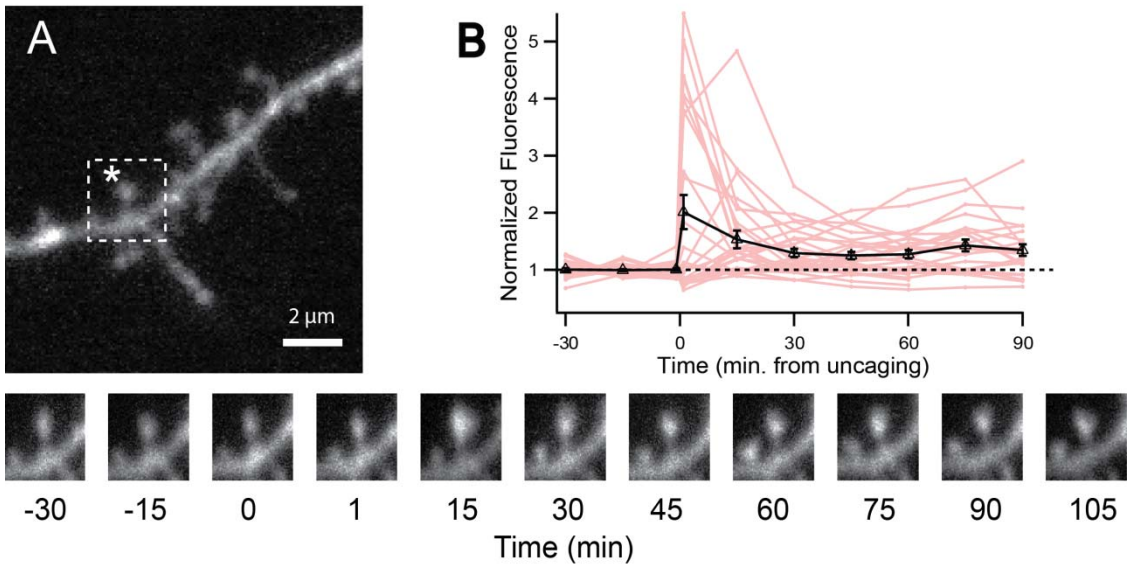

Figure 2.2

Structural plasticity of CA1 dendritic spines elicited by glutamate uncaging in acute slice.

(A) Two-photon image of a CA1 apical dendrite showing the location of uncaging (asterisk) adjacent to an individual spine for structural plasticity assay. Lower panel shows summed image stacks from the spine of interest over time, expressed as minutes from uncaging protocol (60 @ 1 Hz, pulse duration = 0.6 ms). (B) Spines increase in size following uncaging of MNI glutamate. Dashed line indicates no change. Pink lines – individual spines; black triangles – average ± SEM (n = 29).

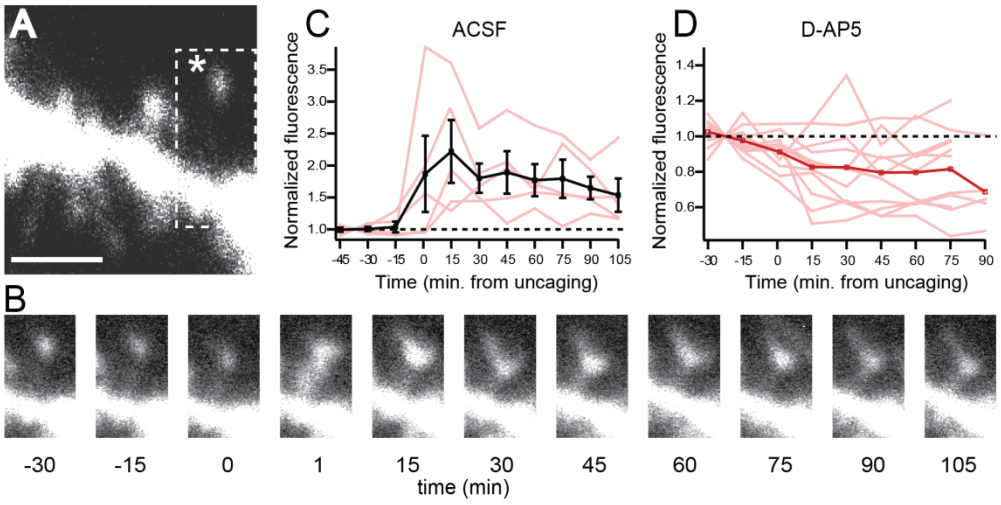

Figure 2.3

Structural plasticity of CA3 dendritic spines elicited by glutamate uncaging in acute slice requires NMDARs.

(A) Two-photon image of a CA3 apical dendrite showing the location of uncaging (asterisk) adjacent to an individual spine. Scale bar represents 2 μm. (B and C) Glutamate uncaging induces structural plasticity in CA3 spines in ACSF (B) but not in the presence of 100 μM D-AP5 (C). Dashed line indicates no change. Pink lines - individual spines; black squares – average ± SEM in ACSF (n = 5); red squares – average in D-AP5 ± SEM (n = 11). (D) Summed image stacks from the spine from shown in A. (ACSF group) show an increase in fluorescence and a change in spine head morphology after uncaging.

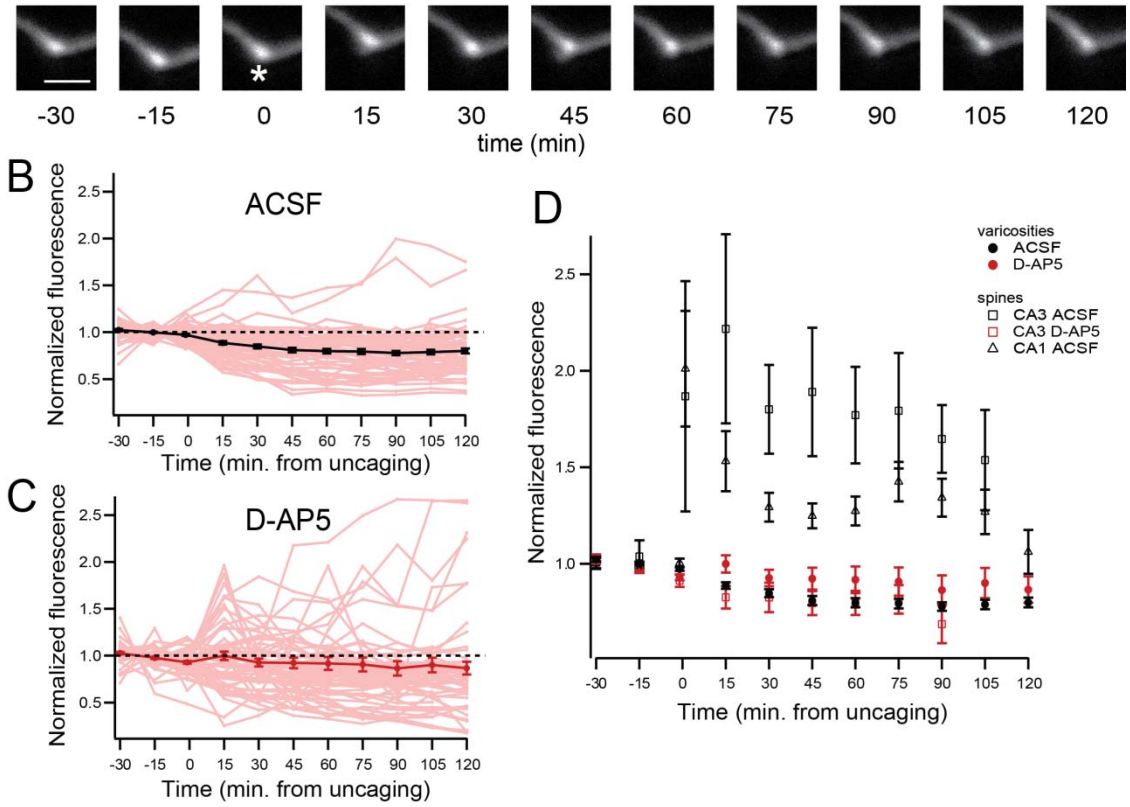

Figure 2.4

Axon varicosities do not increase in size following glutamate uncaging.

(A) Summed image stacks from an example CA3 varicosity over time. Asterisk indicates uncaging position. Scale bar represents 2 μm. (B and C) CA3 axon varicosities do not increase in size following uncaging of MNI glutamate in ACSF with or without D-AP5 (60 @ 1 Hz, pulse duration = 0.6 ms). Group data for CA3 varicosity fluorescence over time for experiments with ACSF only (B), or with 100 μM D-AP5 (C). Dashed line indicates no change. Pink lines – individual varicosities; black circles – average ± SEM in ACSF (n = 61); red circles – average ± SEM in D-AP5, (n = 65). (D) Summary graph of all uncaging experiments. Increases in fluorescence were observed in CA3 and CA1 spines in ACSF. CA3 spine growth was inhibited by 100 μM D-AP5. Varicosity fluorescence followed a similar time course in the presence or absence of D-AP5, and was similar to CA3 spines in D-AP5.

CHAPTER 3.

DISTRIBUTION OF EXTRACELLULAR GLUTAMATE IN THE NUCLEUS ACCUMBENS

Delia N. Chiu and Craig E. Jahr

Vollum Institute, Oregon Health and Science University

Neuroscience Graduate Program, Oregon Health and Science University

Portland, OR USA

Foreword

Dr. Melissa Herman laid the groundwork for this chapter when she was a graduate student in the lab. Her paper *Extracellular Glutamate Concentration in Hippocampal Slice* (2007) provided the idea for the experiments in Figure 3.1, as well as the means to interpret the results (Supplemental Figure 3.1). I also repeated an experiment from her paper for Figure 3.6. Analysis of most of the imaging data would not have been possible without the help of Dr. Brett Carter, who wrote the IGOR macros and functions that were used or modified by me.

Introduction

Fast excitatory synaptic transmission in the CNS is mediated predominantly by glutamate. However, pathological levels of glutamate can activate enough neuronal glutamate receptors to cause cell death. In addition, AMPA receptors (AMPARs) and NMDA receptors (NMDARs) desensitize rapidly (Colquhoun, Jonas, and Sakmann, 1992; Silver, Colquhoun, Cull-Candy, and Edmonds, 1996; Trussell, Thio, Zorumski, and Fischbach, 1988), suggesting that normal receptor function depends on limited exposure to glutamate (Diamond, 2001). Glutamate transporters, or excitatory amino acid transporters (EAATs), take up glutamate from the extracellular space, maintain low ambient glutamate levels, and thereby preserve glutamate signaling integrity and prevent excitotoxicity.

EAAT thermodynamics predict uptake efficient enough to attain an extracellular equilibrium concentration of less than 2 nM (Tzingounis and Wadiche, 2007; Zerangue and Kavanaugh, 1996). Measurements of the average extracellular concentration of glutamate in acute brain slices range from 25 to 90 nM (Cavelier and Attwell, 2005; Herman and Jahr, 2007; Le Meur, Galante, Angulo, and Audinat, 2007), which reflects a steady-state resulting from a balance of release and uptake. However, estimates from *in vivo* microdialysis and biosensors are much higher, ranging from 0.2 to 35 μM (Dash, Douglas, Vyazovskiy, Cirelli, and Tononi, 2009; De Bundel et al., 2011).

One possible explanation for this discrepancy is the existence of compartments, maintained by inhomogeneous densities of EAATs, such that the extracellular non-synaptic space is exposed to a much higher concentration of glutamate, while synapses remain protected by nearby EAATs (Moussawi, Riegel, Nair, and Kalivas, 2011). Modulation of the non-synaptic glutamate concentration has been reported to be instrumental in drug withdrawal behaviors (Moussawi et al., 2001). Ultrastructural evidence for this radical

compartmentalization of EAATs is lacking (Danbolt, 2001; Ventura and Harris, 1999), however, and studies of differential activation of receptors in the two compartments in slice have yielded contradictory results (Herman, Nahir, and Jahr, 2011; Wu, Grebenyuk, McHugh, Rusakov, and Semyanov, 2012).

We chose to further investigate extracellular glutamate in acute slices of the nucleus accumbens (NAc), where values as high as 6 μM have been reported (Miguéns et al., 2008). We measured tonic activation of NMDARs in recordings from medium spiny neurons (MSNs) in acute slices from rat NAc and found a degree of activation consistent with ~30 nM glutamate. To address a controversy as to whether extrasynaptic NMDARs are preferentially activated by ambient glutamate, we used two-photon calcium imaging to monitor activation of NMDARs in the spines and dendritic shafts of MSNs. Using variance analysis we found infrequent calcium excursions in spines that were consistent with calcium influx through NMDARs. In contrast, we found no evidence of calcium influx through dendritic NMDARs. Furthermore, we were unable to find evidence of extracellular compartments that contain widely divergent concentrations of glutamate.

Materials and Methods

Slice preparation

Coronal slices (300 μm) were prepared from Sprague Dawley rats (Charles River, MA) of either sex (PND 14-20, unless otherwise noted) according to protocols approved by the Oregon Health and Science University Institutional Animal Care and Use Committee. Animals were deeply anesthetized with isoflurane and decapitated. Brains were quickly removed and placed in ice-cold solution containing the following (in mM): 110 choline chloride, 7 $MgCl_2$, 2.5 KCl, 1.25 KH_2PO_4, 0.5 $CaCl_2$, 25 $NaHCO_3$, 10 glucose, 3 Na-pyruvate, and 11 Na-ascorbate (saturated with 95% O_2/5% CO_2). The slices were cut using a VibroSlicer (Leica VT1200S, Leica Instruments, Nussloch, Germany)and transferred to a 36°C recovery chamber containing artificial cerebrospinal fluid (ACSF) composed of (in mM): 119 NaCl, 2.5 KCl, 2.0 $CaCl_2$, 1.0 $MgCl_2$, 1.0 NaH_2PO_4, 26.2 $NaHCO_3$, 11 glucose, 3 Na-pyruvate, and 1.3 Na-ascorbate (saturated with 95% O_2/5% CO_2). After 30 min at 36°C slices were maintained at room temperature for 1-5 hours before use.

Whole-cell recordings

Slices were superfused with the above ACSF with 0.5 μM tetrodotoxin (TTX), 10 μM 2,3-dioxo-6-nitro-1,2,3,4-tetrahydrobenzo[f]quinoxaline-7-sulfonamide (NBQX), 20 μM D-serine, and 50 μM picrotoxin. Voltage-sensitive calcium channels (VSCCs) were blocked with 100 μM $CdCl_2$ (Fig. 3.1) or 20 μM mibefradil and 20 μM nimodipine (imaging experiments). Drugs were applied using a four-way manifold connected to a single-barrel flow pipe (545 μm inner diameter) positioned ~700 um upstream from the cell soma (Herman and Jahr, 2007). All experiments were done at 32°C.

Borosilicate glass patch pipettes (World Precision Instruments, Sarasota,FL; 3.5–5 MΩ) were filled with an internal solution containing the following (in mM): 135 Cs-methanesulfonate, 8 NaCl, 10 HEPES, 4 Mg-ATP, 0.4 Na-GTP, 0.24 Fluo-5F, and 0.01 Alexa 594 hydrazide. In standing current experiments (Fig. 3.1), Alexa 594 was omitted, and Fluo-5F was replaced by 0.1 mM EGTA. In frame scan experiments (Fig. 3.4), 4 mM EGTA was added to the internal solution.

Medium spiny neurons (MSNs) in the nucleus accumbens core were visually identified with differential interference contrast optics (Zeiss, Thornwood, NY). Whole-cell recordings were obtained using an Axon Multiclamp 700B amplifier (Molecular Devices, Sunnyvale, CA), using custom software (T.A. Pologruto and B.L. Sabatini) written in MATLAB (MathWorks, Natick, MA). Physiological data were acquired at 5 kHz and filtered at 2 kHz.

Imaging

Imaging and uncaging were performed on a custom-built two-photon laser scanning microscope using an Olympus (Melville, NY) upright microscope and objective (60×, 1.0 NA) and two Chameleon Ti:Sapphire lasers (Coherent, Santa Clara, CA). Lasers were tuned to 840 and 725 nm for excitation and uncaging, respectively. Green and red fluorescence was collected by photomultipliers (H8224 H8224P-40 or H10770PA-40, Hamamatsu Photonics, Hamamatsu, Japan) in epi- and transfluorescence pathways using a 565 dichroic mirror and 525/50 and 620/60 band-pass filters (Chroma Technology, Brattleboro, VT). Images (2 ms/line) were acquired using custom software written in MATLAB. Image acquisition occurred no sooner than 20 minutes after attaining the whole-cell configuration to allow for equilibration of dye. All regions of interest (ROIs) were proximal to the cell soma (≤ 100 μm).

For glutamate uncaging experiments, external solution containing MNI glutamate (5 mM) and glutamic-pyruvic transaminase (GPT; 5 units/μl) was applied to the slice via patch pipette. Uncaging pulses were 0.6 ms in duration. In trials not used for analysis, laser intensity was chosen for each spine such that the response was readily apparent but not saturating (data not shown).

Variance analysis

Calcium transient amplitude was calculated as the mean of 22 points, beginning with the first point after depolarization. With VSCCs and calcium-permeable AMPARs blocked, the variance of the amplitude of calcium transients is the sum of three components (Sabatini and Svoboda, 2000):

$$\sigma^2_{\text{total}} = \sigma^2_{\text{NMDAR}} + \sigma^2_{\text{shot noise}} + \sigma^2_{\text{dark noise}}$$

Dark noise was measured by analyzing pixels from the first 40 ms of acquisitions, when the laser was shuttered. The mean dark pixel value was multiplied by the number of pixels in each ROI and subtracted from the fluorescence signal to get raw Fluo-5F fluorescence, which was used for subsequent analysis.

Shot noise was calibrated at the end of each recording by acquiring 50-100 images of the patch pipette at varying laser intensities. Because the calcium concentration in a small volume of the barrel of the pipette is assumed to be stable, trial-to-trial fluctuations in fluorescence at a given laser intensity are due to shot noise and dark noise alone. The mean and the variance of all pixel values at each intensity were plotted to construct the shot noise calibration curve. The slope of the curve, α, was used to determine the expected contribution of shot noise to total variance given the mean fluorescence.

Statistical analysis

Data were analyzed using IGOR (Wavemetrics) and Excel (Microsoft, Seattle, WA) and are expressed as mean ± SEM. Significance was determined using Wilcoxon matched-pairs signed-ranks test, Mann-Whitney, or paired Student's t-test, $p < 0.05$.

Results

Tonic activation of NMDA receptors is consistent with a sub-micromolar glutamate concentration

We performed whole-cell recordings from MSNs in the NAc core. Cells displayed a standing outward current when held at +40 mV in the presence of NBQX, TTX, and picrotoxin. Application of 100 μM D-AP5 reduced the outward current by 25.1 ± 4.7 pA (n = 19) (Fig. 3.1A, B), indicating that basal extracellular glutamate is present at a concentration high enough to activate a tonic NMDAR-mediated current. Subsequent application of the non-transported NMDAR agonist NMDA (5 μM) evoked an outward current of 234.1 ± 26.3 pA (n = 19) (Fig. 3.1A, B). On average, the amplitude of the current blocked by D-AP5 was 0.118 ± 0.018 times the current evoked by 5 μM NMDA.

The current evoked by 5 μM NMDA is 7.3% of the maximal NMDA-induced current, which was previously determined by measuring the response to a saturating concentration of NMDA (1 mM) in nucleated patches (Supplemental Figure 3.1A; Herman and Jahr, 2007). Multiplying by a factor of 0.073 normalizes the fractional block to the maximal activation by NMDARs. Thus, the D-AP5-sensitive current is 0.118 * 0.073 = 0.0086, or 0.86%, of the maximal current. According to the dose-response curve (EC_{50} = 37.7 μM, n_H = 1.3), the concentration of NMDA that evokes a current of this size is 1 μM.

To convert this concentration of NMDA into a concentration of glutamate, the differences between NMDA and glutamate in both affinity and efficacy must be taken into account. The EC_{50} for glutamate is 20-fold lower than for NMDA ($EC_{50glu}/EC_{50NMDA} \approx 0.048$ Supplemental Figure 3.1A), and glutamate has a higher efficacy than NMDA, as well (max $activation_{NMDA}$/max $activation_{glu} \approx 0.565$; Supplemental Figure 3.1B). Together, these ratios give 0.0271 as the scaling factor used to convert an NMDA concentration to an equipotent concentration of glutamate. Using this scaling factor, we find that tonic activation of

NMDARs in the NAc core corresponds to activation by 27 nM glutamate. This is equivalent to extracellular glutamate in hippocampal neuropil (25 nM; Herman and Jahr, 2007).

This concentration is one hundred times lower than that reported elsewhere (De Bundel et al., 2011; Miguéns et al., 2008). Could a developmental shift account for this difference? We tested this by performing the same experiments with adult rats (8-12 weeks old; 250-385 g). The ratio of the current blocked by 100 μM D-AP5 (30.2 ± 5.6 pA, n = 8) to the current evoked by 5 μM NMDA (254.9 ± 39.3 pA) (Fig. 3.1C) was 0.156 ± 0.047, which corresponds to 1.13% of the maximal response, suggesting that NMDARs in adult NAc core are also exposed to ~25-30 nM glutamate.

Measuring the standing current produced by activation of NMDARs in the absence of evoked synaptic transmission gives an estimate of the average extracellular glutamate concentration, but it does not provide information on its distribution. To gain spatial information about NMDAR activation, we used two-photon laser scanning microscopy.

NMDA receptor openings in the absence of stimulation are infrequent

Because NMDARs are calcium permeable, NMDAR activation can be measured optically by calcium sensitive dyes (Macdermott, Mayer, Westbrook, Smith, and Barker, 1986). This technique has the spatial resolution that whole-cell recording lacks, allowing subcellular detection of receptor activation. Using line scans we monitored intracellular Ca^{2+} excursions in both dendritic spines and shafts during depolarization steps (Fig. 3.2A). To isolate calcium influx through NMDARs, calcium permeable AMPA receptors (AMPARs) and voltage-sensitive calcium channels (VSCCs) were pharmacologically blocked. Release from internal stores was left unblocked, as it is not thought to contribute significantly in these conditions (Mainen, Malinow, and Svoboda, 1999). A step depolarization to +5 mV from -70 mV will relieve the Mg^{2+} block of NMDARs and allow bound receptors to pass

calcium. Indeed, depolarization (40 ms) resulted in a small increase in calcium in both spines ($\Delta G/R = 0.012 \pm 0.003$) (Fig. 3.2B) and dendrites ($\Delta G/R = 0.016 \pm 0.003$) (Fig. 3.2C).

We next tested whether D-AP5 had an effect on calcium transients in dendritic spines and shafts. If the calcium transients are due to influx through NMDARs, D-AP5 should abolish the transients. While D-AP5 decreased the calcium transient in both spines and dendrites, the effect was not significant (spines: $\Delta G/R = 0.010 \pm 0.003$, $n = 6$, $p = 0.218$; dendrites: $\Delta G/R = 0.015 \pm 0.002$, $n = 6$, $p = 0.296$; Fig. 3.2C).

This result is somewhat paradoxical given the fact that we observe tonic activation of NMDARs in MSNs in whole-cell recordings. One explanation for the lack of a significant D-AP5 effect is that these measurements sample a small fraction of the total receptors on the cell. Detection of few, or even single NMDAR openings, are technically feasible, but such openings should occur rarely given our estimate of 30 nM extracellular glutamate.

In order to address the low signal-to-noise ratio in these measurements, and the fact that we predict infrequent channel openings, we adapted a method of variance analysis described by Sabatini and Svoboda (2000) to measure NMDAR activation.

Variance analysis of calcium signals identifies NMDAR activation

We have seen that D-AP5 decreases the calcium transient in both spines and dendrites, but that the decrease was not significant. Basal calcium in cells is approximately 100 nM (Clapham, 2007; Sabatini et al., 2002). The calcium conductance of NMDARs is ~5 pS and they remain bound for ~100 ms. Given that activation of single VSCCs, which have a calcium conductance of ~5-10 pS but are only open for 1-2 ms, can be resolved by two-photon calcium imaging (Sabatini and Svoboda, 2000), a rise in calcium caused by NMDAR activation should be detectable compared to baseline. If NMDARs are activated only rarely, this would explain the lack of effect on the average fluorescence. Variance is a more sensitive

measure of fluctuations, such as those that would be caused by NMDAR openings in a subset of the trials.

NMDAR openings are only one source of variance, however. Shot noise and dark noise also contribute to trial-to-trial variability in the amplitude of the calcium signal. In order to isolate the contribution of NMDAR-mediated calcium excursions, we calculated the total variance for all trials for each ROI (i.e. spine and parent dendrite) in each condition (Fig. 3.3), as well as the amount of variance that shot noise and dark noise are expected to contribute. If total variance and expected variance match closely, we can conclude that the calcium concentration in the ROI remained stable, whether for a particular time period (e.g. t = 40–80 ms), structure (e.g. spine versus dendrite), or condition (e.g. all trials in the presence of D-AP5).

We applied variance analysis to measurements of Fluo-5F fluorescence in order to resolve NMDAR activation by extracellular glutamate in spines and dendrites. For the first 40 ms of each line scan, the laser remained shuttered to calculate dark noise. At t = 40 ms, the shutter was opened and fluorescence at -70 mV was measured, providing a basal calcium signal. At t = 80 ms, the cell was depolarized to +5 mV for 40 ms (Fig. 3.3).

In control solution, total variance matched expected variance closely at -70 mV in both spines and dendrites (spines: total variance = 108.73 ± 1.08% of expected variance, n = 8; dendrites: 111.68 ± 0.89% of expected variance, n = 7) (Fig. 3.4). During depolarization to +5 mV, however, variance increased in spines only (spines: total variance = 147.25 ± 20.07% of expected variance, n = 8; p = 0.0078; dendrites: total variance = 110.14 ± 0.80% of expected variance, n = 7; p = 0.4375).

In the presence of D-AP5, total variance in both spines and dendrites was the same at -70 mV and at +5 mV (spines: total variance = 108.65 ± 4.60% of expected variance at -70 mV, total variance = 109.10 ± 2.52% of expected variance at +5 mV, n = 3; dendrites:

total variance = 111.89 ± 1.86% of expected variance at -70 mV, total variance = 112.22 ± 2.84% of expected variance at +5 mV, n = 3). We have not yet repeated the experiment enough to test the significance of these results, but the preliminary results indicate that D-AP5 blocks the increase in spine variance at +5 mV.

Taken together, these results demonstrate that variance is largest when NMDARs are not blocked by Mg^{2+} or D-AP5. They also confirm our prediction that NMDARs are the main biological source of variance in our calcium measurements.

Activation of single NMDARs can be detected by calcium imaging

Activation of NMDARs by two-photon uncaging of glutamate can be detected using calcium imaging. We uncaged glutamate on MSN spines such that the resulting calcium transient was easily distinguishable from those in interleaved trials without an uncaging pulse. Application of the high-affinity, slowly unbinding NMDAR antagonist, R-CPP (2 μM; Benveniste and Mayer, 1991) abolished the response (Fig. 3.5). Uncaging pulses were delivered during washout of the drug in order to measure the calcium signal during recovery.

In one of the four spines tested, recovery from R-CPP inhibition was incomplete, preventing further analysis. In the other three, we observed recovery of the calcium transient that suggests activation of increasing numbers of NMDARs. First, the amplitude increased compared to interleaved control trials. Importantly, the amplitude of these washout responses was smaller than the baseline uncaging response. Second, there were failures interspersed with these smaller amplitude uncaging responses after washout. Third, the amplitude of washout responses increased with time.

We interpret this as evidence that slow unblock of the high affinity antagonist leaves increasing numbers of NMDARs available for activation by uncaging. The fact that the smallest responses are interspersed with failures suggests that these responses are the result

of the activation of a small number of NMDARs, because as receptor availability increases, the likelihood of all NMDARs failing to open in response to the uncaging pulse should decrease. If this is the case, then it is possible that the smallest washout responses could represent individual NMDAR openings.

Additional experiments to test this interpretation are necessary (see Discussion). However, we compared the putative single NMDAR uncaging responses ($\Delta[Ca]_{recovery}$) to the non-evoked, small-amplitude calcium transients ($\Delta[Ca]_{ambient\ glu}$) that occasionally occur in control conditions in the preceding experiments (Figs. 3.3, 3.4). We found that the amplitudes of $\Delta[Ca]_{recovery}$ and $\Delta[Ca]_{ambient\ glu}$ were similar ($\Delta G/R = 0.102 \pm 0.07$ and 0.096 ± 0.015, respectively; $p = 0.177$). Furthermore, instances of $\Delta[Ca]_{ambient\ glu}$ were observed very rarely in spines tested; on average in 2% of all trials in control ACSF (20/1086). If those trials are deleted from the variance calculation, the resulting variance matches that predicted from dark and shot noise. This indicates that these rare events are the result of NMDA channel openings in the spines. Such events were never observed in the dendritic shafts.

The lack of dendritic responses likely results from very high density of NMDAR expression in spines and much lower expression density in dendrites, though quantification of expression levels in these two compartments is not possible using calcium imaging. If there are very few dendritic receptors, the dendrites will not be reliable sensors of extrasynaptic ambient glutamate. Thus, to determine whether there is a glutamate concentration gradient across extracellular compartments produced by glutamate transporters protecting synaptic receptors, we inhibited glutamate transporters while measuring calcium transients in dendrites and spines.

TBOA increases receptor activation

To directly address the question of compartmentalization, we monitored spine calcium while applying the glutamate transporter antagonist TBOA. As transport is blocked, extracellular glutamate will gain access to all compartments of the extracellular space equally. If extrasynaptic extracellular glutamate is 1-6 μM (Miguéns et al., 2008), then synaptic NMDAR activation should rapidly increase with transport block. To calibrate the effect of TBOA on NMDAR activation, we compared application of 100 μM TBOA, a concentration that will produce maximal block of EAATs (Bergles, Tzingounis, and Jahr, 2002) to application of NMDA (20 μM).

Though NMDA has a 20-fold higher EC_{50} and is less efficacious than glutamate NMDARs (Cavelier and Attwell, 2005; Herman and Jahr, 2007), 20 μM NMDA evoked a larger calcium increase than 100 μM TBOA. This suggests that at the time of TBOA wash-in extracellular glutamate in all compartments is less than 1 μM.

Activation of NMDARs depolarizes MSNs

It has been proposed that low micromolar glutamate is required for normal MSN and NAc function (Baker et al., 2003; Moussawi et al., 2011b). Though our measurements using electrophysiology and calcium imaging are not consistent with this proposal, we wanted to measure the effect 1 μM glutamate would have on MSN function. Because exogenous glutamate is taken up by EAATs in the slice, we used 30 μM NMDA to activate NMDARs. This concentration is less than the EC_{50} concentration for NMDA (37.7 μM) and is equipotent to 1.5 μM glutamate (Herman and Jahr, 2007), which is below others' estimates of extracellular glutamate.

Antagonists were omitted from the bath solution, as was D-serine, which was otherwise present at a saturating dose (10-20 μM) in order to promote NMDAR activation

upon binding glutamate. Cells were current-clamped in order to monitor membrane potential. Superfusion of the slice with 30 μM NMDA (Fig. 3.6) resulted in depolarization (15.62 ± 1.18 mV, n = 7). All cells tested began spiking within 30 seconds of NMDA application, and eventually entered in a quiescent, unresponsive state (Fig. 3.6). This increase in excitability followed by spike accommodation indicates that activation of glutamate receptors by agonist at half-maximal concentration for NMDARs is not permissive for normal MSN function. Taken together with our finding that significant compartmentalization of the extracellular space into regions of high and low tonic glutamate concentrations does not occur, this suggests that, on average, extracellular glutamate is well below an EC_{50} concentration for NMDARs.

Discussion

The concentration of basal extracellular glutamate in the NAc is sub-micromolar

We find that the concentration of extracellular glutamate in the nucleus accumbens is ~30 nM. This result is in the range of extracellular glutamate predicted by EAAT thermodynamics, receptor desensitization parameters, and measurements in hippocampal neuropil.

Frequency of spontaneous NMDAR openings in steady-state glutamate concentrations

We used calcium imaging to monitor NMDAR activation. Averages of many measurements of spine fluorescence are altered very little by the low frequency and the small amplitude of events mediated by single NMDAR openings, making definitive statements about the level of ambient glutamate difficult. Determining the absolute frequency of NMDAR events by counting events is problematic because the duration of NMDAR channel openings can vary tremendously from one event to another. Very short channel openings will be missed because calcium influx will not result in a measureable increase in fluorescence. Despite this, even if short duration openings are missed, the very low frequency of unmistakable fluorescence events can be interpreted qualitatively as evidence of low resting glutamate in the synaptic cleft.

Variance analysis of NMDAR-mediated changes in the calcium concentration revealed that the modest average increase in calcium in spines and dendrites during depolarization in control ACSF had different origins. In spines, rare large events, while adding little to the small average increase, led to greater fluctuations across measurements and therefore greater variance. The lack of large fluctuations in dendrites resulted in smaller variance, suggesting that more frequent but smaller rises in calcium results in the average

increase. We interpret this as evidence that calcium was not entering through NMDARs located in dendritic shafts at the site of imaging, but rather that calcium-bound dye was diffusing to the site of imaging, most likely from more numerous NMDAR events on the large number of surrounding spines.

In the study by Semyanov's group, the effect of D-AP5 on the calcium signal in the dendrite was central to their conclusion that extracellular glutamate is higher around dendrites than spines (Wu et al., 2012). Taking diffusion of calcium-bound dye into account, we propose that the dendrite is not sampling a higher glutamate concentration than the spine, but is sampling, via its spines, many more sites that are exposed to the low glutamate concentration.

Lack of evidence for steep concentration gradient

If transporters maintain a concentration gradient between synaptic and extrasynaptic compartments, such that synaptic extracellular glutamate is less than 100 nM and the average concentration, as determined by microdialysis, is 1-3 μM, we can make two predictions: 1) Many receptors in the extrasynaptic compartment would have a high probability of being bound and open or desensitized; and 2) inhibition of transporters would lead to activation of synaptic receptors comparable to direct application of 1-3 μM glutamate.

One way to test the first prediction is to do simultaneous calcium measurements in spines and dendritic shafts. If the two structures are exposed to two different glutamate concentrations, this could be reflected in the amount of NMDAR activation observed. Two groups have previously measured the effect of D-AP5 on calcium transients in hippocampal CA1 spines versus dendrites (Herman et al., 2011; Wu et al., 2012) and reported conflicting results. We repeated the experiment in MSNs and found, in agreement with both of the

previous studies, that there is a very small NMDAR-mediated calcium signal in both spines and dendrites when magnesium block is relieved during line scan.

The second prediction is perhaps more straightforward but testing it is technically challenging. Blocking uptake leads to a pooling of glutamate, but the time course will depend on wash-in of the drug and its access to transporters. In addition, global calcium rises due to activation of many receptors, over the entire cell surface, making it difficult to detect single events.

By measuring the increase in Fluo-5F fluorescence in both 100 μM TBOA and 20 μM NMDA, we were able make a qualitative comparison. Once uptake is blocked by TBOA, extracellular glutamate has equal access to all receptors, synaptic and extrasynaptic. This is the also true of NMDA, which is not transported by EAATs, and therefore has equal access to all receptors. Calcium rose in dendrites and spines during application of TBOA and during application of NMDA, but 20 μM NMDA led to a greater increase. We concluded that this concentration of NMDA must be greater than the concentration of extracellular glutamate in the extrasynaptic space; as 20 μM NMDA is equipotent to 1 μM glutamate, this argues against the presence of >1 μM glutamate in the extracellular space.

It is noteworthy that in some studies in the NAc, extrasynaptic receptors are defined as those receptors that are activated by synaptic release only when uptake is blocked (Botelho et al., 2014; Shen, Scofield, Boger, Hensley, and Kalivas, 2014). This is not consistent with the idea of transporters protecting the synaptic space from the outside, but rather with the function of transporters to limit spillover of synaptically released glutamate to nearby synapses.

High extracellular glutamate affects physiology and receptor availability

The concentration of extracellular glutamate has implications not only for behavior, but for receptor function. While it is likely that levels of extracellular glutamate change under pathological conditions (Baker et al., 2003; Moussawi, Zhou, et al., 2011), it is difficult to reconcile their estimates of with the results shown in Figure 3.6 in which a concentration of NMDA equivalent to 1.5 μM glutamate results in a large depolarization that ultimately causes accommodation and lack of further neuronal activity. Such quiescent neurons probably exist surrounding microdialysis probes and in severe ischemic tissue.

Given the literature on extracellular glutamate and addiction, it is unclear how to interpret their results. Are qualitative changes in extracellular glutamate concentration real, but the concentrations lower? Or is there another explanation for findings attributed to changes in extracellular glutamate over the ranges reported?

Sun and colleagues recently examined the effect of a gap in astrocyte coverage on the steady-state extracellular glutamate concentration (Sun, Shchepakin, Kalachev, and Kavanaugh, 2014). Assuming a Gaussian-shaped region of impaired uptake due to damage from probe insertion, they calculated that extracellular glutamate would reach 3-10 μM inside the probe, depending on the rate of leak (i.e. glutamate efflux). Microdialysis studies could thus be reporting pathologically high extracellular glutamate not because the probes cause more efflux, but because they are creating a space of extremely reduced uptake.

Future experiments

There are several experiments that need to be repeated before the work presented in this chapter can be considered complete. Variance analysis was done on a set of eight spines from seven cells. Though each set of line scans represents over 150 trials, the data set is not complete. In particular, the effect of D-AP5 was only tested in three out of eight spines.

Similarly, the experiment using washout of CPP to observe single NMDAR openings was only repeated four times. The amplitude of the uncaging-evoked transients was variable before CPP. A larger, more stable response before CPP addition would strengthen the argument that small successes represent single receptor openings. In addition, I will have control experiments to test whether the calcium response to uncaging remains stable for the number of observations necessary (30-60) to perform the experiment with CPP.

Also, one way to test the validity of the interpretation of the CPP experiment is to repeat the experiment with a higher concentration of external calcium in the ACSF. If the size of the first response(s) during CPP-washout scale with calcium concentration, that would be evidence that we are detecting single NMDAR responses. That would provide not only a rationale for identifying spontaneous calcium excursions as NMDAR-mediated in the experiments discussed in this chapter, but would also stand alone as an important demonstration of the resolution of the technique.

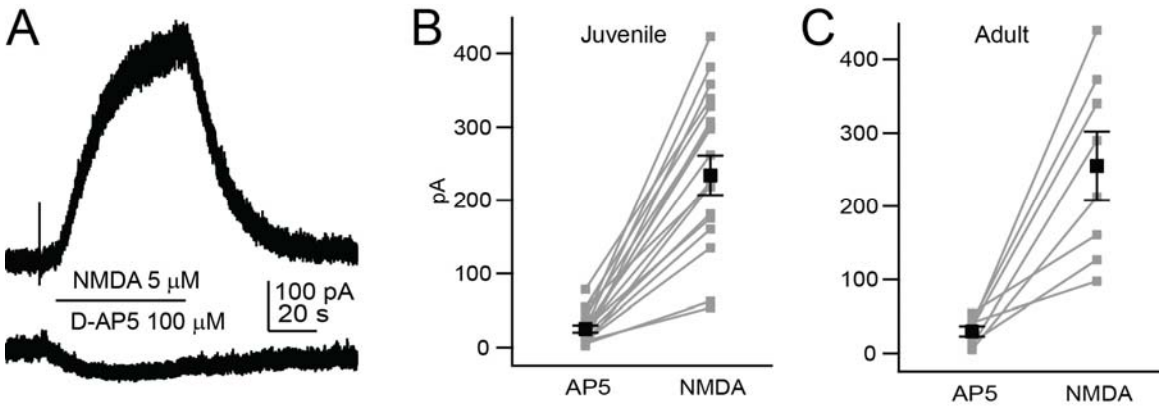

Figure 3.1

Standing and evoked NMDA receptor currents at +40 mV.

(A) Current traces from MSN voltage-clamped at +40 mV show outward current evoked by 5 μM NMDA (upper trace) and inhibition of a standing current by 100 μM D-AP5 (lower trace). (B and C) Comparison of the current blocked by 100 μM D-AP5 and the current evoked by 5 μM NMDA in young (P20-25) rats (B) and adult (8-12 weeks) rats (C). Individual pairs in grey, averages ± SEM in black.

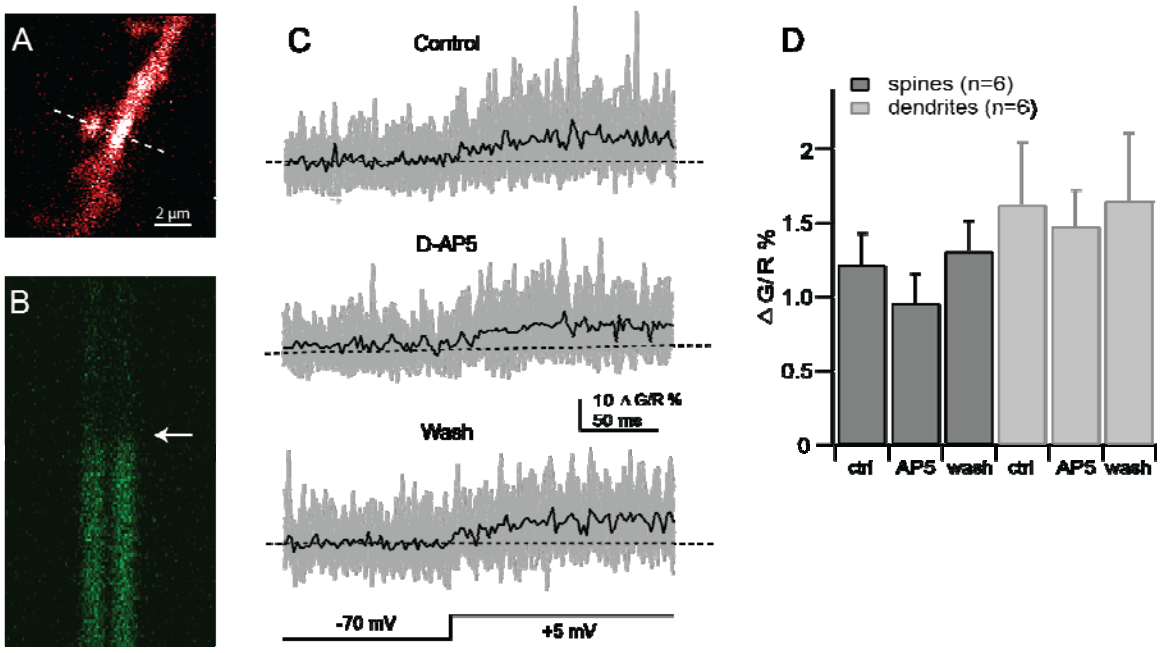

Figure 3.2

D-AP5 does not significantly alter CA^{2+} influx at +5 mV.

(A) Frame scan showing MSN dendrite filled with Alexa 594. Dashed line indicates position of line scan shown in B. (B) Fluo-5F fluorescence increases upon depolarization to +5 mV (indicated by arrow) in spine and dendrite. (C) Fluorescence traces from a single MSN spine during depolarization to +5 mV in control (upper), in 100 µM D-AP5 (middle), and after washout of D-AP5 (lower) (14 trials in each condition). Command voltage indicated underneath. Individual traces in grey, averages in black. (D) Fluo-5F fluorescence averages. D-AP5 did not significantly reduce the amplitude of calcium responses to depolarization in spines ($p = 0.435$) or dendrites ($p = 0.592$). Error bars represent SEM.

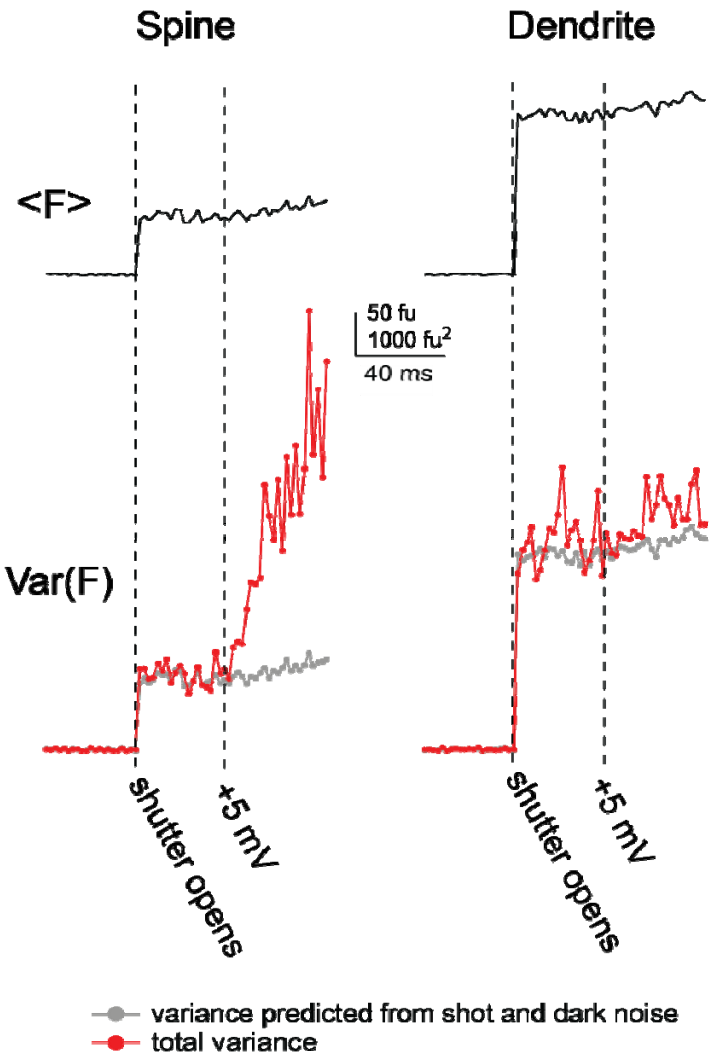

Figure 3.3

Spine variance reflects infrequent, stochastic NMDAR openings.

Mean Fluo-5F fluorescence <F> from 160 trials from spine and dendrite pair are shown in the upper traces (black). For the first 40 ms of each trial, the shutter was closed. At t = 40 ms (first dashed line), the shutter was opened and fluorescence at -70 mV was measured. At t = 80 ms (second dashed line), the cell was depolarized to +5 mV for 40 ms. Variance Var(F) of the measurements is shown below. The total variance, shown in red, was calculated for each time point. Grey traces show variance predicted from dark noise and shot noise of the mean signal.

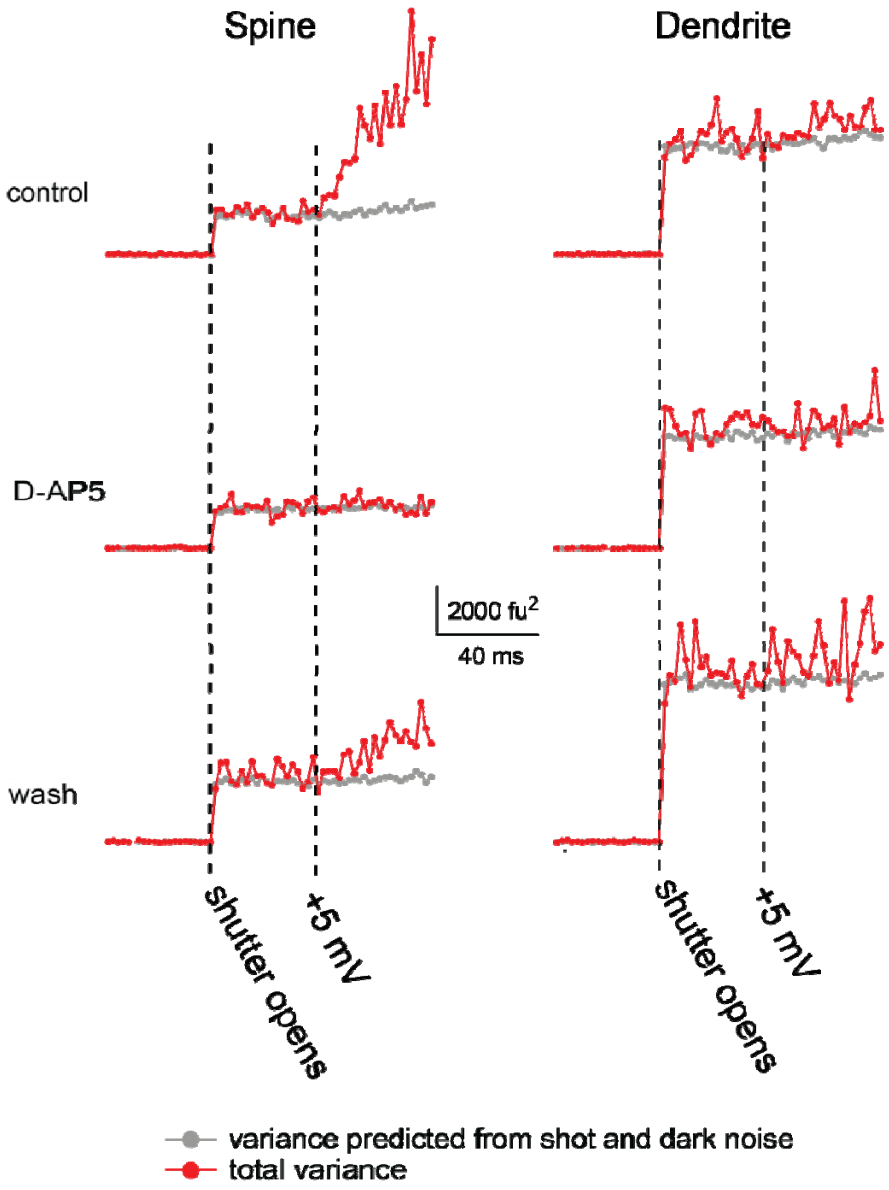

Figure 3.4

D-AP5 blocks variance increase.

Variance of calcium signals in spine and dendrite pair in control (upper), in 100 μM D-AP5 (middle), and after washout of D-AP5 (lower) (n = 160 in each condition). Comparison of total variance (red) and predicted variance (grey) shows variance of calcium signals decreases in the presence of D-AP5 in spines, but not dendrites.

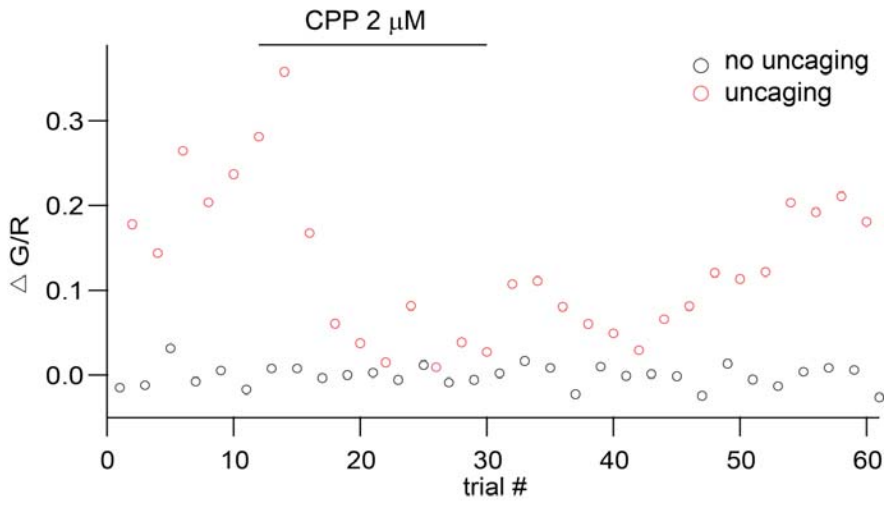

Figure 3.5

NMDAR openings in spines result in measurable fluorescence increases.

Diary plot showing calcium responses in a single MSN spine to uncaging MNI glutamate (red) and without uncaging (black) during application and washout of 2 μM R-CPP.

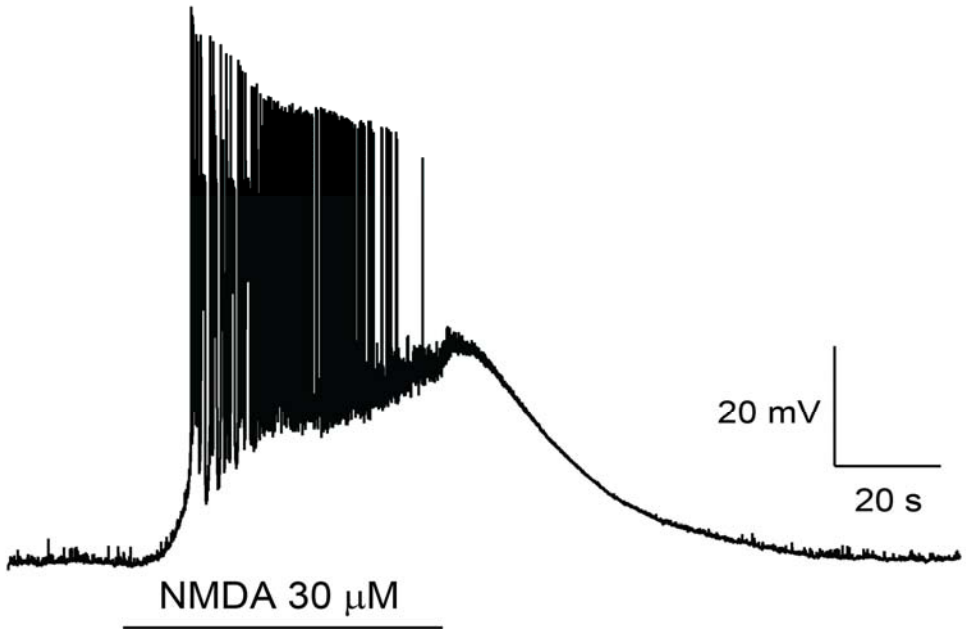

Figure 3.6

MSNs accommodate in the equivalent of 1.5 μM glutamate.

Current clamp recording from MSN in ACSF without TTX, picrotoxin, NBQX, or D-serine. V_{rest} = -76 mV. Flow pipe application of 30 μM NMDA induced depolarization and burst firing. Firing ceased after 40 seconds in the continued presence of NMDA.

.

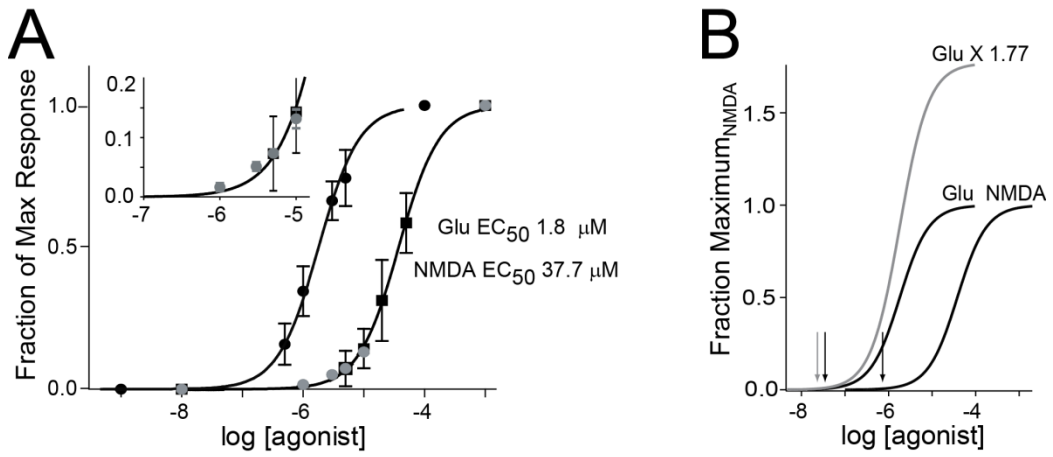

Supplemental Figure 3.1

Dose-response curves for glutamate and NMDA.

Modified from Herman and Jahr, 2007, Figure 2.

(A) Semi-log plot of whole-cell (n = 6; gray circles) and nucleated patch (n = 6) current responses from application of NMDA (black squares) and glutamate (Glu; black circles; 0.5, 1, 3, 5, 100 μM; n = 6). Nucleated patch response were normalized to the maximum response. Whole-cell responses were scaled by the mean nucleated patch response to 5 μM NMDA. Line through NMDA responses is the nonlinear regression fit with Hill equation of nucleated patch dose responses (EC_{50} of 37.7 μM; $n_H = 1.3$). Line through glutamate responses is the NMDA fit shifted by EC_{50Glu}/EC_{50NMDA}. Inset, Expansion of low concentration portion of NMDA dose–response curve. (B) Dose–response curves from A with glutamate-fit curve scaled by the efficacy ratio of 1.77. Arrows indicate the concentrations of glutamate and NMDA required to evoke currents of the same amplitude as that induced by ambient glutamate in hippocampus.

Summary

In Chapter One the search for direct evidence of presynaptic NMDARs ultimately led to the finding that release from cerebellar MLIs is enhanced by subthreshold depolarization. Paired recordings showed that postsynaptic IPSCs were larger when presynaptic action potentials were preceded by a subthreshold depolarization. Two-photon calcium imaging of individual MLI axon varicosities revealed a small increase in calcium in trials with subthreshold current injection. Inhibition of VSCCs abolished the increase in subthreshold calcium, as did bath application of EGTA-AM. We concluded that VSCCs are activated by subthreshold depolarization in the axon and that the calcium influx from that activation leads to the enhancement of release.

A question about axons and long-term plasticity motivated the work presented in chapter two. Is there a presynaptic structural correlate of long-term plasticity? The experiments were relatively straightforward once I was able to get sparse expression of GFP in the hippocampus with in utero electroporation. Using dendritic spines as a positive control was important for the interpretation of the results, as were collecting and analyzing data in a condition-blind manner.

As with most studies, but perhaps particularly in the case of a negative result, there are still questions to be answered with regard to the second chapter. A recent report of presynaptic structural plasticity (Meyer et al., 2014) is not easily reconciled with the results I have presented in Chapter Two. However, differences between the techniques used can be examined to identify the reason for the discrepancy, which could in turn shed light on the mechanisms governing both functional and structural plasticity.

The motivation for the work in the third chapter was to resolve the outstanding question of whether extracellular glutamate in the nucleus accumbens is distributed

differently than in hippocampus. I used endogenous NMDA receptors as high-affinity glutamate sensors to measure extracellular glutamate, a technique employed by Melissa Herman in an earlier study (Herman and Jahr, 2007). Tonic activation of NMDARs was low compared to maximal activation by NMDA, suggesting low extracellular glutamate.

I also used two-photon calcium imaging to monitor calcium excursions, as had been done in hippocampus both by our lab and others (Herman et al., 2011; Wu et al., 2012). Imaging experiments addressed compartmentalization by simultaneously monitoring NMDAR activation in two different compartments. However, NMDAR activation was difficult to measure using average data because openings were infrequent. To overcome this I adapted Sabatini and Svoboda's use of variance analysis on calcium signals, which they used to count calcium channels in dendritic spines (Sabatini and Svoboda, 2000), to NMDA receptor activation.

Transport block removed the main sink for extracellular glutamate, leading to increased activation of NMDARs, but was not consistent with flooding of synaptic spaces with a high concentration of glutamate. Finally, application of NMDA in the absence of any antagonists provided an example of the cellular response to high extracellular glutamate. Taken together, these results indicate that extracellular glutamate in the nucleus accumbens is ~30 nM, and is not present at micromolar concentrations in the extracellular space. This is especially important given the high glutamate affinity of NMDARs, as well as their roles in coincidence detection and calcium signaling. As shown by the dose-response curves for glutamate, this should minimize the number of receptors in a desensitized state, thereby promoting synaptic transmission.

References

Alle, H., and Geiger, J. (2006). Combined analog and action potential coding in hippocampal mossy fibers. Science *311,* 1290-1293.

Atluri, P.P., and Regehr, W.G. (1996). Determinants of the time course of facilitation at the granule cell to Purkinje cell synapse. J. Neurosci. *16*, 5661–5671.

Atluri, P.P., and Regehr, W.G. (1998). Delayed release of neurotransmitter from cerebellar granule cells. J. Neurosci. *18*, 8214–8227.

Awatramani, G.B., Price, G.D., and Trussell, L.O. (2005). Modulation of transmitter release by presynaptic resting potential and background calcium levels. Neuron *48*, 109–121.

Baker, D. a, McFarland, K., Lake, R.W., Shen, H., Tang, X.-C., Toda, S., and Kalivas, P.W. (2003). Neuroadaptations in cystine-glutamate exchange underlie cocaine relapse. Nat. Neurosci. *6*, 743–749.

Becker, N., Wierenga, C.J., Fonseca, R., Bonhoeffer, T., and Nägerl, U.V. (2008). LTD induction causes morphological changes of presynaptic boutons and reduces their contacts with spines. Neuron *60*, 590–597.

Benveniste, M., and Mayer, M.L. (1991). Kinetic analysis of antagonist action at N-methyl-D-aspartic acid receptors. Two binding sites each for glutamate and glycine. Biophys. J. *59*, 560–573.

Bergles, D.E., Tzingounis, A. V, and Jahr, C.E. (2002). Comparison of coupled and uncoupled currents during glutamate uptake by GLT-1 transporters. J. Neurosci. *22*, 10153–10162.

Bischofberger, J., Geiger, J.R.P., and Jonas, P. (2002). Timing and efficacy of Ca2+ channel activation in hippocampal mossy fiber boutons. J. Neurosci. *22*, 10593–10602.

Bollmann, J.H., Sakmann, B., and Borst, J.G. (2000). Calcium sensitivity of glutamate release in a calyx-type terminal. Science *289*, 953–957.

Borst, J.G., and Sakmann, B. (1996). Calcium influx and transmitter release in a fast CNS synapse. Nature *383*, 431–434.

Borst, J.G., and Sakmann, B. (1998). Facilitation of presynaptic calcium currents in the rat brainstem. J. Physiol. *513 (Pt 1)*, 149–155.

Botelho, E.P., Wang, E., Chen, J.Y., Holley, S., Andre, V., Cepeda, C., and Levine, M.S. (2014). Differential Synaptic and Extrasynaptic Glutamate-Receptor Alterations in Striatal Medium-Sized Spiny Neurons of Aged YAC128 Huntington's Disease Mice. PLoS Curr. *6*.

Bourne, J.N., and Harris, K.M. (2011). Coordination of size and number of excitatory and inhibitory synapses results in a balanced structural plasticity along mature hippocampal CA1 dendrites during LTP. Hippocampus *21*, 354–373.

Bourne, J.N., Kirov, S.A., Sorra, K.E., and Harris, K.M. (2007). Warmer preparation of hippocampal slices prevents synapse proliferation that might obscure LTP-related structural plasticity. Neuropharmacology *52*, 55–59.

Brenowitz, S.D., and Regehr, W.G. (2007). Reliability and heterogeneity of calcium signaling at single presynaptic boutons of cerebellar granule cells. J. Neurosci. *27*, 7888–7898.

Bucurenciu, I., Kulik, A., Schwaller, B., Frotscher, M., and Jonas, P. (2008). Nanodomain coupling between Ca2+ channels and Ca2+ sensors promotes fast and efficient transmitter release at a cortical GABAergic synapse. Neuron *57*, 536–545.

Bucurenciu, I., Bischofberger, J., and Jonas, P. (2010). A small number of open Ca2+ channels trigger transmitter release at a central GABAergic synapse. Nat. Neurosci. *13*, 19–21.

De Bundel, D., Schallier, A., Loyens, E., Fernando, R., Miyashita, H., Van Liefferinge, J., Vermoesen, K., Bannai, S., Sato, H., Michotte, Y., et al. (2011). Loss of system x(c)- does not induce oxidative stress but decreases extracellular glutamate in hippocampus and influences spatial working memory and limbic seizure susceptibility. J. Neurosci. *31*, 5792–5803.

Cavelier, P., and Attwell, D. (2005). Tonic release of glutamate by a DIDS-sensitive mechanism in rat hippocampal slices. J. Physiol. *564*, 397–410.

Christie, J.M., and Jahr, C.E. (2008). Dendritic NMDA receptors activate axonal calcium channels. Neuron *60*, 298–307.

Christie, J.M., and Jahr, C.E. (2009). Selective expression of ligand-gated ion channels in L5 pyramidal cell axons. J. Neurosci. *29*, 11441–11450.

Clapham, D.E. (2007). Calcium signaling. Cell *131*, 1047–1058.

Colquhoun, D., Jonas, P., and Sakmann, B. (1992). Action of brief pulses of glutamate on AMPA/kainate receptors in patches from different neurones of rat hippocampal slices. J. Physiol. *458*, 261–287.

Cornish, J.L., and Kalivas, P.W. (2000). Glutamate transmission in the nucleus accumbens mediates relapse in cocaine addiction. J. Neurosci. *20*, RC89.

Cuttle, M.F., Tsujimoto, T., Forsythe, I.D., and Takahashi, T. (1998). Facilitation of the presynaptic calcium current at an auditory synapse in rat brainstem. J. Physiol. *512 (Pt 3)*, 723–729.

Dalva, M.B., McClelland, A.C., and Kayser, M.S. (2007). Cell adhesion molecules: signalling functions at the synapse. Nat. Rev. Neurosci. *8*, 206–220.

Danbolt, N.C. (2001). Glutamate uptake. Prog. Neurobiol. *65*, 1–105.

Dash, M.B., Douglas, C.L., Vyazovskiy, V. V, Cirelli, C., and Tononi, G. (2009). Long-term homeostasis of extracellular glutamate in the rat cerebral cortex across sleep and waking states. J. Neurosci. *29*, 620–629.

Diamond, J.S. (2001). Neuronal glutamate transporters limit activation of NMDA receptors by neurotransmitter spillover on CA1 pyramidal cells. J. Neurosci. *21*, 8328–8338.

Diana, M.A., and Marty, A. (2003). Characterization of depolarization-induced suppression of inhibition using paired interneuron--Purkinje cell recordings. J. Neurosci. *23*, 5906–5918.

Dittman, J.S., Kreitzer, A.C., and Regehr, W.G. (2000). Interplay between facilitation, depression, and residual calcium at three presynaptic terminals. J. Neurosci. *20*, 1374–1385.

Dodt, H.-U., Eder, M., Schierloh, A., and Zieglgänsberger, W. (2002). Infrared-guided laser stimulation of neurons in brain slices. Sci. STKE *2002*, pl2.

Elias, G.M., and Nicoll, R.A. (2007). Synaptic trafficking of glutamate receptors by MAGUK scaffolding proteins. Trends Cell Biol. *17*, 343–352.

Felmy, F., Neher, E., and Schneggenburger, R. (2003). Probing the intracellular calcium sensitivity of transmitter release during synaptic facilitation. Neuron *37*, 801–811.

Fisher-Lavie, A., and Ziv, N.E. (2013). Matching dynamics of presynaptic and postsynaptic scaffolds. J. Neurosci. *33*, 13094–13100.

Forti, L., Pouzat, C., and Llano, I. (2000). Action potential-evoked Ca2+ signals and calcium channels in axons of developing rat cerebellar interneurones. J. Physiol. *527 (Pt 1)*, 33–48.

Geiger, J.R., and Jonas, P. (2000). Dynamic control of presynaptic Ca(2+) inflow by fast-inactivating K(+) channels in hippocampal mossy fiber boutons. Neuron *28*, 927–939.

Glitsch, M., and Marty, a (1999). Presynaptic effects of NMDA in cerebellar Purkinje cells and interneurons. J. Neurosci. *19*, 511–519.

Heidelberger, R., Heinemann, C., Neher, E., and Matthews, G. (1994). Calcium dependence of the rate of exocytosis in a synaptic terminal. Nature *371*, 513–515.

Herman, M. a, and Jahr, C.E. (2007). Extracellular glutamate concentration in hippocampal slice. J. Neurosci. *27*, 9736–9741.

Herman, M. a, Nahir, B., and Jahr, C.E. (2011). Distribution of extracellular glutamate in the neuropil of hippocampus. PLoS One *6*, e26501.

Hori, T., and Takahashi, T. (2009). Mechanisms underlying short-term modulation of transmitter release by presynaptic depolarization. J. Physiol. *587*, 2987–3000.

Hruska, M., and Dalva, M.B. (2012). Ephrin regulation of synapse formation, function and plasticity. Mol. Cell. Neurosci. *50*, 35–44.

Ichtchenko, K., Hata, Y., Nguyen, T., Ullrich, B., Missler, M., Moomaw, C., and Südhof, T.C. (1995). Neuroligin 1: A splice site-specific ligand for β-neurexins. Cell *81*, 435–443.

Jinno, S., Jeromin, A., Roder, J., and Kosaka, T. (2002). Immunocytochemical localization of neuronal calcium sensor-1 in the hippocampus and cerebellum of the mouse, with special reference to presynaptic terminals. Neuroscience *113*, 449–461.

Jinno, S., Jeromin, A., and Kosaka, T. (2004). Expression and possible role of neuronal calcium sensor-1 in the cerebellum. Cerebellum *3*, 83–88.

Kessels, H.W., and Malinow, R. (2009). Synaptic AMPA receptor plasticity and behavior. Neuron *61*, 340–350.

Kole, M.H.P., Letzkus, J.J., and Stuart, G.J. (2007). Axon initial segment Kv1 channels control axonal action potential waveform and synaptic efficacy. Neuron *55*, 633–647.

LaLumiere, R.T., and Kalivas, P.W. (2008). Glutamate release in the nucleus accumbens core is necessary for heroin seeking. J. Neurosci. *28*, 3170–3177.

Li, L., Bischofberger, J., and Jonas, P. (2007). Differential gating and recruitment of P/Q-, N-, and R-type Ca2+ channels in hippocampal mossy fiber boutons. J. Neurosci. *27*, 13420–13429.

Lisman, J.E., and Harris, K.M. (1993). Quantal analysis and synaptic anatomy--integrating two views of hippocampal plasticity. Trends Neurosci. *16*, 141–147.

Llano, I., Tan, Y.P., and Caputo, C. (1997). Spatial heterogeneity of intracellular Ca2+ signals in axons of basket cells from rat cerebellar slices. J. Physiol. *502 (Pt 3)*, 509–519.

Llano, I., González, J., Caputo, C., Lai, F.A., Blayney, L.M., Tan, Y.P., and Marty, A. (2000). Presynaptic calcium stores underlie large-amplitude miniature IPSCs and spontaneous calcium transients. Nat. Neurosci. *3*, 1256–1265.

Lu, T., and Trussell, L.O. (2000). Inhibitory transmission mediated by asynchronous transmitter release. Neuron *26*, 683–694.

Macdermott, A.B., Mayer, M.L., Westbrook, G.L., Smith, S.J., and Barker, J.L. (1986). NMDA-receptor activation increases cytoplasmic calcium concentration in cultured spinal cord neurones. Nature *321*, 519-522.

Mainen, Z.F., Malinow, R., and Svoboda, K. (1999). Synaptic calcium transients in single spines indicate that NMDA receptors are not saturated. Nature *399*, 151–155.

Matsuzaki, M., Honkura, N., Ellis-Davies, G.C.R., and Kasai, H. (2004). Structural basis of long-term potentiation in single dendritic spines. Nature *429*, 761–766.

Mejia-Gervacio, S., Collin, T., Pouzat, C., Tan, Y.P., Llano, I., and Marty, A. (2007). Axonal speeding: shaping synaptic potentials in small neurons by the axonal membrane compartment. Neuron *53*, 843–855.

Metz, A.E., Jarsky, T., Martina, M., and Spruston, N. (2005). R-type calcium channels contribute to afterdepolarization and bursting in hippocampal CA1 pyramidal neurons. J. Neurosci. *25*, 5763–5773.

Le Meur, K., Galante, M., Angulo, M.C., and Audinat, E. (2007). Tonic activation of NMDA receptors by ambient glutamate of non-synaptic origin in the rat hippocampus. J. Physiol. *580*, 373–383.

Meyer, D., Bonhoeffer, T., and Scheuss, V. (2014). Balance and Stability of Synaptic Structures during Synaptic Plasticity. Neuron *82*, 430–443.

Miguéns, M., Del Olmo, N., Higuera-Matas, a, Torres, I., García-Lecumberri, C., and Ambrosio, E. (2008). Glutamate and aspartate levels in the nucleus accumbens during cocaine self-administration and extinction: a time course microdialysis study. Psychopharmacology (Berl). *196*, 303–313.

Moussawi, K., Riegel, A., Nair, S., and Kalivas, P.W. (2011a). Extracellular glutamate: functional compartments operate in different concentration ranges. Front. Syst. Neurosci. *5*, 94.

Moussawi, K., Zhou, W., Shen, H., Reichel, C.M., See, R.E., Carr, D.B., and Kalivas, P.W. (2011b). Reversing cocaine-induced synaptic potentiation provides enduring protection from relapse. Proc. Natl. Acad. Sci. U. S. A. *108*, 385–390.

Müller, M., Felmy, F., and Schneggenburger, R. (2008). A limited contribution of Ca2+ current facilitation to paired-pulse facilitation of transmitter release at the rat calyx of Held. J. Physiol. *586*, 5503–5520.

Müller, M., Goutman, J.D., Kochubey, O., and Schneggenburger, R. (2010). Interaction between facilitation and depression at a large CNS synapse reveals mechanisms of short-term plasticity. J. Neurosci. *30*, 2007–2016.

Otsu, Y., Shahrezaei, V., Li, B., Raymond, L.A., Delaney, K.R., and Murphy, T.H. (2004). Competition between phasic and asynchronous release for recovered synaptic vesicles at developing hippocampal autaptic synapses. J. Neurosci. *24*, 420–433.

Palay, S.L., and Chan-Palay, V. Cerebellar cortex: cytology and organization. Springer-Verlag; New York: 1974.

Rae, J., Cooper, K., Gates, P., and Watsky, M. (1991). Low access resistance perforated patch recordings using amphotericin B. J. Neurosci. Methods *37*, 15–26.

Sabatini, B.L., and Regehr, W.G. (1997). Control of neurotransmitter release by presynaptic waveform at the granule cell to Purkinje cell synapse. J. Neurosci. *17*, 3425–3435.

Sabatini, B.L., and Svoboda, K. (2000). Analysis of calcium channels in single spines using optical fluctuation analysis. Nature *408*, 589–593.

Sabatini, B.L., Oertner, T.G., and Svoboda, K. (2002). The Life Cycle of Ca2+ Ions in Dendritic Spines. Neuron *33*, 439–452.

Schikorski, T., and Stevens, C.F. (1997). Quantitative Ultrastructural Analysis of Hippocampal Excitatory Synapses. J. Neurosci. *17*, 5858–5867.

Schneggenburger, R., and Neher, E. (2000). Intracellular calcium dependence of transmitter release rates at a fast central synapse. Nature *406*, 889–893.

Scott, R., Ruiz, A., Henneberger, C., Kullmann, D.M., and Rusakov, D.A. (2008). Analog modulation of mossy fiber transmission is uncoupled from changes in presynaptic Ca2+. J. Neurosci. *28*, 7765–7773.

Shen, H., Scofield, M.D., Boger, H., Hensley, M., and Kalivas, P.W. (2014). Synaptic glutamate spillover due to impaired glutamate uptake mediates heroin relapse. J. Neurosci. *34*, 5649–5657.

Shu, Y., Hasenstaub, A., Duque, A., Yu, Y., and McCormick, D. a (2006). Modulation of intracortical synaptic potentials by presynaptic somatic membrane potential. Nature *441*, 761–765.

Silver, R.A., Colquhoun, D., Cull-Candy, S.G., and Edmonds, B. (1996). Deactivation and desensitization of non-NMDA receptors in patches and the time course of EPSCs in rat cerebellar granule cells. J. Physiol. *493 (Pt 1)*, 167–173.

Sun, W., Shchepakin, D., Kalachev, L. V, and Kavanaugh, M.P. (2014). Glutamate transporter control of ambient glutamate levels. Neurochem. Int. *73*, 146–151.

Svoboda, K. (2004). Do spines and dendrites distribute dye evenly? Trends Neurosci. *27*, 445–446.

Takeichi, M. (1988). The cadherins: cell-cell adhesion molecules controlling animal morphogenesis. Development *102*, 639–655.

Tang, Y., Schlumpberger, T., Kim, T., Lueker, M., and Zucker, R.S. (2000). Effects of mobile buffers on facilitation: experimental and computational studies. Biophys. J. *78*, 2735–2751.

Tottene, A., Moretti, A., and Pietrobon, D. (1996). Functional diversity of P-type and R-type calcium channels in rat cerebellar neurons. J. Neurosci. *16*, 6353–6363.

Trigo, F.F., Bouhours, B., Rostaing, P., Papageorgiou, G., Corrie, J.E.T., Triller, A., Ogden, D., and Marty, A. (2010). Presynaptic miniature GABAergic currents in developing interneurons. Neuron *66*, 235–247.

Trussell, L.O., Thio, L.L., Zorumski, C.F., and Fischbach, G.D. (1988). Rapid desensitization of glutamate receptors in vertebrate central neurons. Proc. Natl. Acad. Sci. U. S. A. *85*, 4562–4566.

Tsujimoto, T., Jeromin, A., Saitoh, N., Roder, J.C., and Takahashi, T. (2002). Neuronal calcium sensor 1 and activity-dependent facilitation of P/Q-type calcium currents at presynaptic nerve terminals. Science *295*, 2276–2279.

Turecek, R., and Trussell, L.O. (2001). Presynaptic glycine receptors enhance transmitter release at a mammalian central synapse. Nature *411*, 587–590.

Tzingounis, A. V, and Wadiche, J.I. (2007). Glutamate transporters: confining runaway excitation by shaping synaptic transmission. Nat. Rev. Neurosci. *8*, 935–947.

Umeda, T., Ebihara, T., and Okabe, S. (2005). Simultaneous observation of stably associated presynaptic varicosities and postsynaptic spines: morphological alterations of CA3–CA1 synapses in hippocampal slice cultures. Mol. Cell. Neurosci. *28*, 264–274.

Ventura, R., and Harris, K.M. (1999). Three-dimensional relationships between hippocampal synapses and astrocytes. J. Neurosci. *19*, 6897–6906.

Vincent, P., and Marty, A. (1996). Fluctuations of inhibitory postsynaptic currents in Purkinje cells from rat cerebellar slices. J. Physiol. *494 (Pt 1)*, 183–199.

Wu, L.G., and Borst, J.G. (1999). The reduced release probability of releasable vesicles during recovery from short-term synaptic depression. Neuron *23*, 821–832.

Wu, L.G., Borst, J.G., and Sakmann, B. (1998). R-type Ca2+ currents evoke transmitter release at a rat central synapse. Proc. Natl. Acad. Sci. U. S. A. *95*, 4720–4725.

Wu, Y.W., Grebenyuk, S., McHugh, T.J., Rusakov, D.A., and Semyanov, A. (2012). Backpropagating Action Potentials Enable Detection of Extrasynaptic Glutamate by NMDA Receptors. Cell Rep. *1*, 495–505.

Yang, X., Hou, D., Jiang, W., and Zhang, C. (2014). Intercellular protein-protein interactions at synapses. Protein Cell *5*, 420–444.

Zerangue, N., and Kavanaugh, M.P. (1996). Flux coupling in a neuronal glutamate transporter. Nature *383*, 634–637.

Zucker, R.S., and Regehr, W.G. (2002). Short-term synaptic plasticity. Annu. Rev. Physiol. *64*, 355–405.